JGR Solid Earth

RESEARCH ARTICLE
10.1029/2022JB025177

Coupling Crustal-Scale Rift Architecture With Passive Margin Salt Tectonics: A Geodynamic Modeling Approach

Leonardo M. Pichel[1], Ritske S. Huismans[1], Robert Gawthorpe[1], Jan Inge Faleide[2], and Thomas Theunissen[1]

[1]Department of Earth Science, University of Bergen, Bergen, Norway, [2]Department of Geosciences, University of Oslo, Oslo, Norway

Key Points:

- We use geodynamic models of lithospheric extension to investigate post-rift salt tectonics for different types of rifted margins
- Narrow margins form partially isolated salt sub-basins associated with prominent relief, limited seaward translation but major diapirism
- Wide margins form large salt basins with low relief, major seaward salt expulsion, nappe advance, updip extension and downdip shortening

Supporting Information:

Supporting Information may be found in the online version of this article.

Correspondence to:

L. M. Pichel,
Leonardo.M.Pichel@uib.no

Citation:

Pichel, L. M., Huismans, R. S., Gawthorpe, R., Faleide, J. I., & Theunissen, T. (2022). Coupling crustal-scale rift architecture with passive margin salt tectonics: A geodynamic modeling approach. *Journal of Geophysical Research: Solid Earth*, *127*, e2022JB025177. https://doi.org/10.1029/2022JB025177

Received 13 JUL 2022
Accepted 28 OCT 2022

Author Contributions:

Conceptualization: Leonardo M. Pichel, Ritske S. Huismans, Robert Gawthorpe
Formal analysis: Leonardo M. Pichel
Funding acquisition: Ritske S. Huismans
Investigation: Leonardo M. Pichel
Methodology: Leonardo M. Pichel, Ritske S. Huismans, Thomas Theunissen
Project Administration: Ritske S. Huismans, Robert Gawthorpe, Jan Inge Faleide

Abstract Continental rifted margins are often associated with widespread, thick evaporite (i.e., salt) deposits and pronounced salt tectonics. The majority of salt basins formed during the latest stages of rifting, prior to continental breakup. We use 2D thermo-mechanical finite element modeling of lithospheric extension to investigate the interplay between rifted margin architecture, late syn-rift salt deposition, and post-rift salt tectonics. We focus on four different types of continental margins: (a) narrow, (b) intermediate, (c) wide, and (d) ultra-wide margins. We evaluate the: (a) interplay between laterally variable syn-rift extension, salt deposition and salt tectonics, (b) influence of syn-rift basin architecture on post-rift salt flow, (c) spatial and temporal distribution of salt-related structural domains, and (d) contrasting styles of salt tectonics for different margin types. Narrow and intermediate margins form partially isolated salt basins associated with prominent base-salt relief, limited translation but significant diapirism, and minibasin development. Wide and ultra-wide margins form wide salt basins with subtle base-salt relief that results in significant seaward salt expulsion and overburden translation. These wide margins demonstrate significant updip extension with the development of post-rift normal faults and rollovers, mid-margin translation associated with complex diapirism and downdip diapir shortening. All margins contain a distal salt nappe that varies in width and complexity. We also test the effect of different salt viscosities, relative post-salt progradation rates, and pre-salt sediment thicknesses. The results are comparable to several examples of salt-bearing rifted margins and improve our understanding of their dynamics and on the controls on their salt tectonics variability.

Plain Language Summary Rifting of the continental lithosphere can lead to continental breakup and formation of continental margins, which are often associated with widespread, thick salt basins that deform in a ductile fashion and produce complex geological structures. Most of these basins formed during the latest stages of rifting, prior to continental breakup. We use 2D thermo-mechanical numerical modeling of lithospheric extension to investigate the interplay between rifted margin architecture, late-syn-rift salt and post-rift salt tectonics for four different types of margins: (a) narrow, (b) intermediate, (c) wide, and (d) ultra-wide. We evaluate the interplay between syn-rift extension, salt deposition and deformation, the influence of rift basin architecture on post-rift salt flow, and the contrasting styles and magnitudes of salt deformation for different margin types. Narrow and intermediate margins form isolated salt sub-basins associated with prominent relief, limited seaward translation but significant vertical salt flow. Wide and ultra-wide margins form broad salt basins with subtle relief, significant seaward salt expulsion, updip extension, translation and downdip shortening. All margins contain a distal salt sheet advancing laterally over newly formed oceanic crust. The results can be directly compared to several examples of salt-bearing rifted margins worldwide and provide an improved understanding of their dynamics.

1. Introduction

Continental rifting and breakup are a product of the extension and thinning of the lithosphere and ocean floor spreading (McKenzie, 1978). The style of rifting and margin architecture is generally controlled by the rheology and overall composition of the crust and mantle lithosphere. Strong crust favors narrow rifting whereas weak crust promotes formation of wide rifted margins (Buck, 1991; Huismans & Beaumont, 2011, 2014). Other factors such as the lithospheric thermal state and thickness, inheritance and temporal and spatial variations in rifting kinematics also influence rifted margin architecture (Brune et al., 2014, 2016; Buck, 1991; Huismans & Beaumont, 2002, 2003; Lavier & Manatschal, 2006).

Software: Leonardo M. Pichel, Ritske S. Huismans, Thomas Theunissen
Supervision: Ritske S. Huismans, Robert Gawthorpe, Jan Inge Faleide
Validation: Ritske S. Huismans, Robert Gawthorpe, Jan Inge Faleide
Visualization: Leonardo M. Pichel, Thomas Theunissen
Writing – original draft: Leonardo M. Pichel
Writing – review & editing: Leonardo M. Pichel, Ritske S. Huismans, Robert Gawthorpe, Jan Inge Faleide

Many rifted passive margins are associated with widespread and thick (up to 3–4 km) evaporite (salt) deposits and pronounced salt tectonics (Davison et al., 2012; Kukla et al., 2018; Lentini et al., 2010; Peel, 2014; Rowan, 2014) (Figure 1). Salt deposition can occur during different stages of rifting although the majority and largest salt basins formed during the latest stages of rifting, immediately prior to continental breakup, for example, the

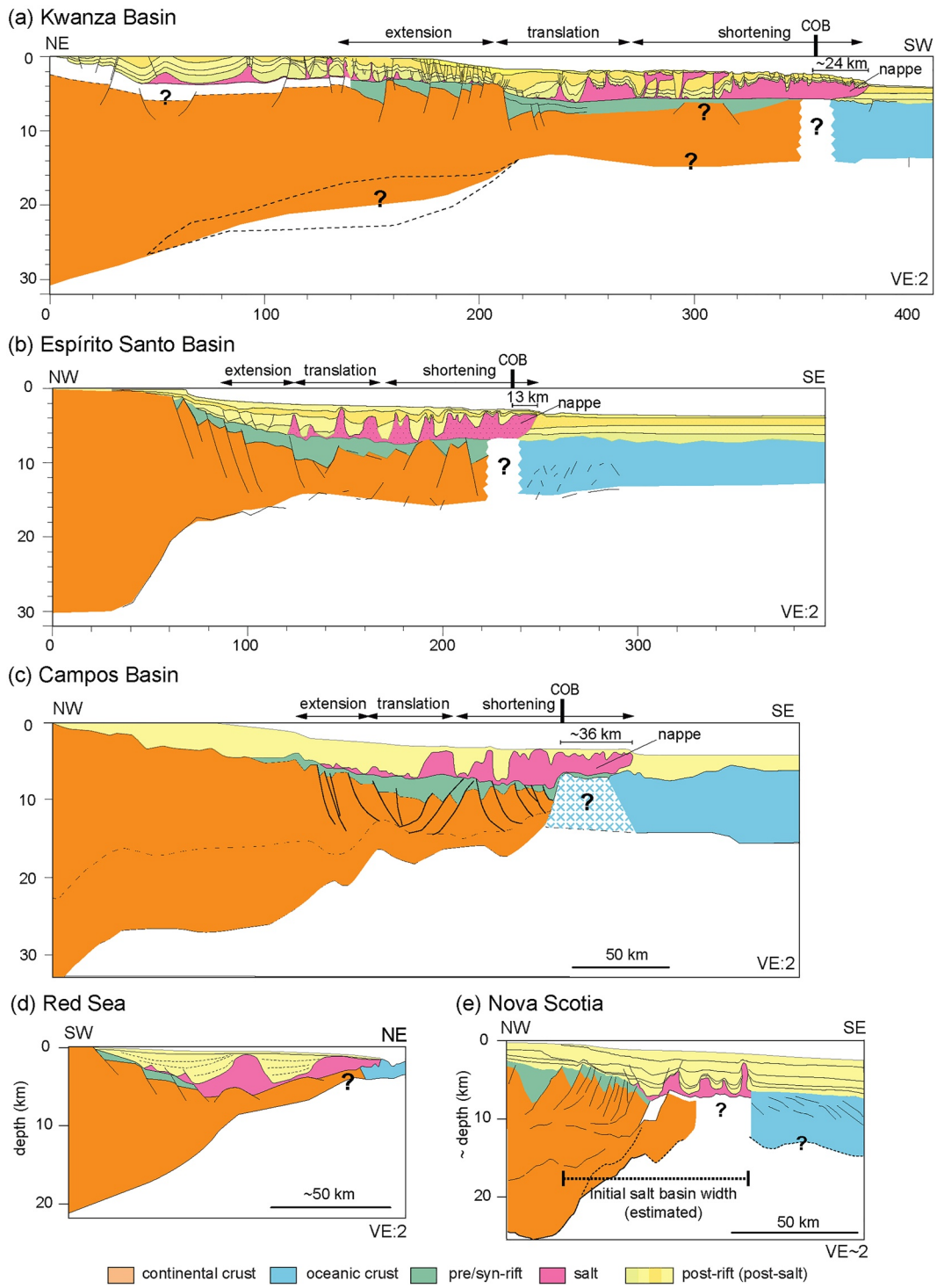

Figure 1. Regional profiles showing crustal-scale architecture and salt structures across (a) Kwanza Basin, Angola, (b) Espirito Santo, Brazil (adapted from Blaich et al. [2011]), and (c) Campos Basin, Brazil (adapted from Zalán et al. [2011]), (d) Southern Red Sea (adapted from Mohriak and Leroy [2013]) and (e) southern Nova Scotia, Canada (adapted from Goteti et al. [2013]).

Gulf of Mexico and South Atlantic salt giants, the Red Sea, NW Africa, and Nova Scotia (Davison et al., 2012; M. P. Jackson & Hudec, 2017; Rowan, 2014, 2020; Tari et al., 2003) (Figure 1). The crustal rift-related architecture and basin infill of these margins and the dimension, geometry, and thickness of their salt basins show considerable variation leading to contrasting styles of salt tectonics.

Many studies have investigated regional salt tectonics along rifted margins (Davison et al., 2012; Deptuck & Kendell, 2017; Gemmer et al., 2004; Hudec & Jackson, 2004; C. A. L. Jackson, Jackson, & Hudec, 2015; Marton et al., 2000; Peel et al., 1995; Pichel et al., 2018, 2019; Tari et al., 2003, 2017). However, very few have analyzed the link between crustal-scale margin architecture, salt deposition, and salt tectonics (Curry et al., 2018; Epin et al., 2021; Kukla et al., 2018; Pichel et al., 2022; Rowan, 2020). This largely results from limitations in seismic imaging of deep crustal geometries, in particular when they underlie thick and/or highly deformed salt, and to the challenges in modeling both lithosphere-scale deformation and sedimentary basin formation including salt tectonics at sufficient resolution in numerical models (Allen & Beaumont, 2016). Goteti et al. (2013) were the first to attempt this by applying forward thermo-mechanical modeling using prescribed and highly simplified rift basin geometries (i.e., rifting was not modeled) to model salt tectonics of early syn-rift salt basins. Allen and Beaumont (2016) expanded on their work by using dynamically evolving numerical models that combined lithospheric extension and syn-rift salt tectonics to examine the differences between early, mid and late syn-rift salt for a single margin type of intermediate width. Allen et al. (2020) then applied the same approach to investigate syn-rift salt tectonics in wide continental margins. While these studies provided insight in understanding syn-rift extension and syn-rift salt deformation, the role of rift architecture and syn-rift salt on long-lived post-rift salt tectonics on continental margins has not yet been addressed.

More recently, Pichel et al. (2022) used 2D thermo-mechanically coupled finite element modeling of lithospheric extension to simulate the syn- and post-rift evolution of late-syn rift salt basins along wide rifted margins. We expand on this work and apply the same numerical modeling approach to investigate the interplay between variable styles of rifted margin, syn-rift basin architecture and consequences for distribution of late syn-rift salt deposits, and post-rift salt tectonics. We focus on four different types of continental margins: (a) narrow, (b) intermediate, (c) wide, and (d) ultra-wide margins. For each of these margins we evaluate: (a) the interplay between laterally variable syn-rift crustal extension, salt deposition, and deformation, (b) the influence of syn-rift basin architecture on post-rift salt flow, (c) the spatial and temporal distribution of salt-related structural domains, and (d) the contrasting styles of salt tectonics for the different margin types.

These models are the first to integrate lithospheric extension with long-lived post-rift salt tectonics along different types of continental margins using geodynamically self-consistent numerical models. The models do not prescribe the geometries of the lithosphere and the salt basins allowing a natural evolution of both syn- and post-rift deformation (cf., Pichel et al., 2022). They also incorporate a more realistic style of post-rift sedimentation and margin progradation using a dynamically evolving depositional profile and present unprecedented detail for salt, syn- and post-rift stratigraphy that can be directly compared to natural examples from various salt-bearing continental margins.

2. Numerical Model Approach and Design

We apply an arbitrary Lagrangian-Eulerian (ALE) finite element approach for the solution of thermo-mechanically coupled, plane strain, incompressible viscous-plastic creeping flows (Erdős et al., 2014; Theunissen & Huismans, 2019; Thieulot, 2011). The model solves the quasi-static force balance equations in two dimensions coupled with the time-dependent heat conservation equation (see Supporting Information S1 for details on numerical modeling method and model setup).

The models present an idealized rheologically layered lithosphere overlying a sublithospheric mantle in a 600 km high and 1,200 km wide model domain (Figure 2) (cf., Theunissen & Huismans, 2019). The lithosphere comprises a 35 km-thick crust and 85 km mantle lithosphere overlying the sublithospheric mantle (Figure 2). The Eulerian grid contains 2,400 and 290 elements in the horizontal and vertical directions, respectively, following an irregular distribution in the vertical direction, which allows for high resolution in the upper crust and the sedi-

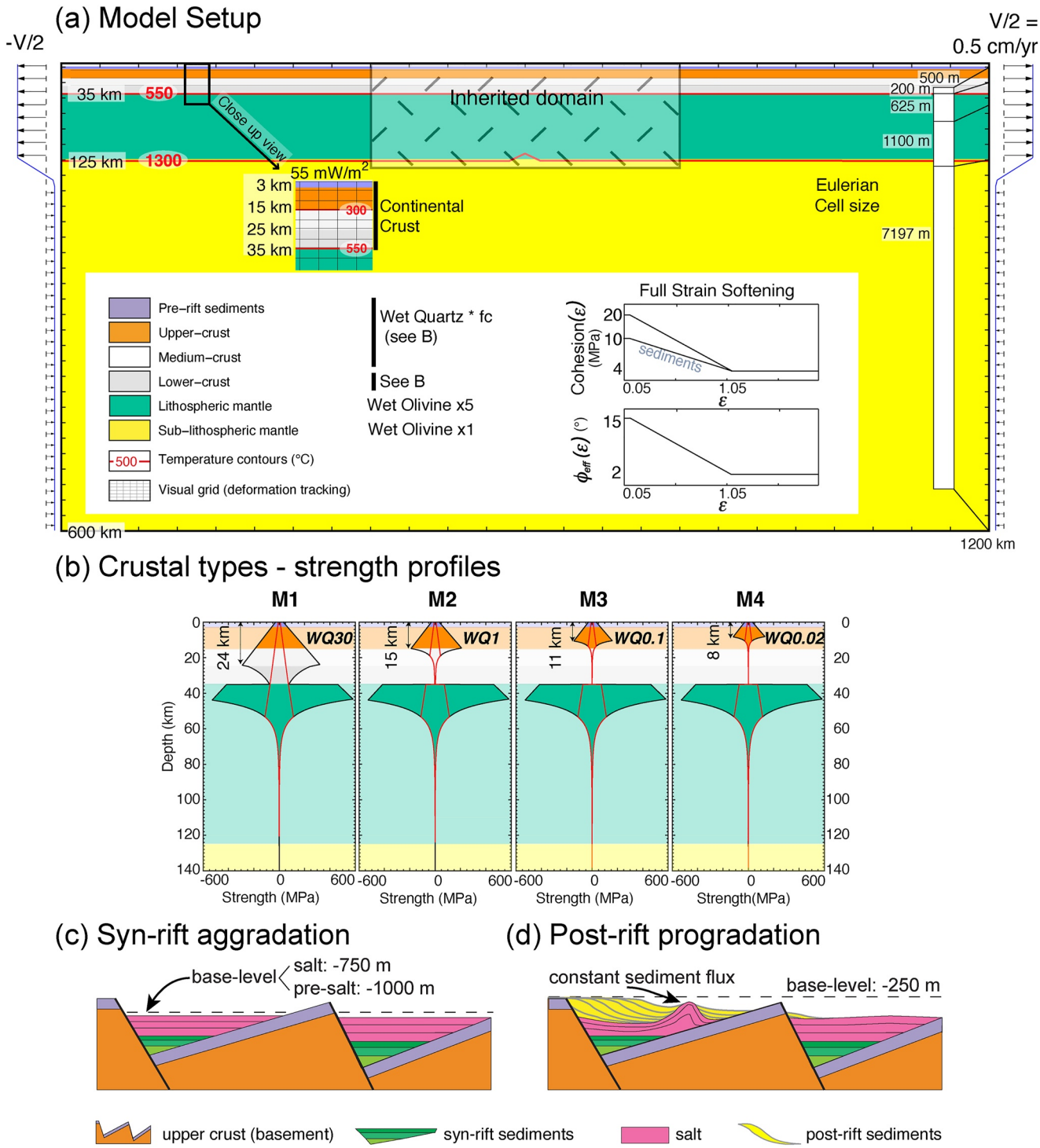

Figure 2. (a) Model setup showing rheological-layered structure, boundary conditions, initial thermal state, and frictional-plastic strain softening conditions. The values used for the mechanical and thermal parameters are listed in Table 1. (b) Diagram illustrating lithosphere strength profiles and different crustal rheologies and strength used in our four main models, M1-4. (c) Schematic diagram illustrating syn-rift aggradation for pre-salt and salt sediments in which sediments aggrade toward local basement minima without diffusion over structural highs. (d) Schematic diagram illustrating post-rift (post-salt) dynamic progradation in which the depositional profile changes in shape and length through time according to the evolving salt topography.

Table 1
Parameters for the Lithosphere-Scale Thermo-Mechanical Models of Salt-Bearing Wide Rifted Margins

Parameter	Symbol	Units	Salt	Sediments	Upper crust (0–25 km)	Lower crust (25–35 km)	Lithospheric mantle	Sub-lithospheric mantle
Rheological parameters								
Effective viscosity range	μ_{eff}	Pa.s	10^{18}, 5×10^{18}, 10^{19}	10^{18}–10^{27}	10^{18}–10^{27}	10^{18}–10^{27}	10^{18}–10^{27}	10^{18}–10^{27}
Angle of internal friction	ϕ_{eff}	—	-	15	15		15	
→ after strain weakening	ϕ_{eff}	—	-	2	2		4	
Initial cohesion	C	MPa	-	10	20		20	
→ after strain weakening	C	MPa	-	4	4		20	
Strain weakening range	—	—	-			0.05–1.05		
Flow law	—	—	-		WQtz[a]		WO[b]	
Scaling factor	f_c	—	-	1	0.1		5	1
Power law exponent	N	—	-	4	4		3	
Activation energy	Q	kJ/mol	-	222.81	222.81		429.83	
Constant	A	Pa^{-n}/s	-		8.574×10^{-28}		1.758×10^{-14}	
Activation volume	V	m^3/mol	-		0.0		15×10^{-6}	
Density at $T_0 = 273$ K	ρ_0	kg/m^3	2,200	2,400	2,750	2,900	3,300	
Thermal parameters								
Thermal conductivity	k	W/m/K		2.25			2.25–5.6	
							2.25–51.46	
Heat capacity	c_p	J/K/kg	803.57		818.18	775.86	681.81	
Thermal diffusivity	K	m^2/s		1.0×10^{-6}			$1–2.5 \times 10^{-6}$	
							$1–22.87 \times 10^{-6}$	
Heat production rate	H	W/m	0.8×10^{-6}		1.12×10^{-6}	0.48×10^{-6}	0	
Thermal expansion	α_T	1/K	3×10^{-5}			3.1×10^{-5}		
Boundary conditions								
Surface temperature	T_{surf}	°C			0			
Pre-rift sediment thickness	$h_{pre\text{-}sed}$	km			3			
Initial Moho depth	d_{moho}	km			35			
Moho temperature	T_{moho}	°C			550			
LAB depth	d_{LAB}	km			125			
LAB temperature	T_{LAB}	°C			1,328			
Basal temperature	T_{LM}	°C			1,520			
Extension velocity	V_{ext}	cm/year			1			

Note. Flow laws are based on power law with creep parameters from wet quartz (Gleason & Tullis, 1995) and wet olivine (Karato & Wu, 1993). Values are given with two digits precision. WQtz, wet quartz; WO, wet olivine; LAB, Lithosphere-Asthenosphere Boundary.
[a]Dislocation creep models for WQtz. [b]Dislocation creep models for WO.

mentary basins. The vertical resolution thus varies from $\Delta z = 200$ m in the first 20 km, $\Delta z = 625$ m between 20 and 70 km, $\Delta z = 1{,}100$ m between 70 and 120 km, and $\Delta z = 7{,}917$ m between 120 and 600 km. The horizontal resolution is 500 m for the entire model. Extensional velocity boundary conditions ($v = \pm 0.5$ cm/year) are applied horizontally to the entire lithosphere, producing an exit flux of model particles that is balanced by a low velocity inflow in the sublithospheric mantle (Figure 2a) (Theunissen & Huismans, 2019). A complete description of the numerical modeling approach and model setup are provided in Supporting Information S1. A list of material parameters is given in Table 1.

The crust is modeled following a wet quartz (WQ) rheology (Gleason & Tullis, 1995) with different scaling factors (f_c) as a means to test different crustal strength profiles (Figure 2) (Theunissen & Huismans, 2019). We use four contrasting crustal rheologies based on the experiments from Theunissen and Huismans (2019) by varying f_c from 30, 1, 0.1, and 0.02 for strong, intermediate, weak, and very weak crust, respectively (Figure 2). These result in distinct thicknesses of the frictional-plastic upper crust that range from 25 km, 15, 11, to 8 km, respectively. This scaling allows the creation of either strong or weak, viscous crust without the complications involving additional flow laws, each with its own uncertainties (Theunissen & Huismans, 2019). This viscous scaling can be either regarded as a measure of the uncertainty in the properties of rocks where flow is dominated by quartz (e.g., wet or dry) or to represent variations in their thermal state and composition (e.g., Huismans & Beaumont, 2011, 2014; Theunissen & Huismans, 2019).

Sedimentation occurs by filling all accommodation between the model surface and a defined base(sea)-level with sediments at each time step. We implement two different styles of sedimentation in our models, aggradation for syn-rift clastics and salt, and post-rift progradation using a dynamic progradation with a constant sediment flux (Theunissen & Huismans, 2019). Aggradation is defined with a horizontal base-level with a vertical position that is adjusted for each main depositional stage, that is, syn-rift clastics and salt deposition (Figure 2c). For the post-rift progradation, instead of prescribing a constant, albeit laterally moving depositional profile defined by half-Gaussian curves (Albertz & Ings, 2012; Allen & Beaumont, 2016; Gemmer et al., 2004; Goteti et al., 2013), we adopt dynamic progradation where deposition is controlled by specifying a constant sediment flux, Q_s, to the basin (e.g., Theunissen & Huismans, 2019, Supporting Information S1). Syn- and post-rift sediments have an average density of 2,400 kg m^{-3}, the salt of 2,200 kg m^{-3}.

The study comprises three sets of models. The first set (M1–M4) utilizes an intermediate salt viscosity and explores the interplay between four distinct crustal geometries and margin types with syn- to post-rift regional salt tectonics. The second set explores the effect of varying syn-rift and salt thickness for a weak crustal rheology. Lastly, a supplementary models set explores the sensitivity to variable salt viscosities. All models include water-load, syn-rift (pre-salt) aggradation at −1 km base-level. The pre-salt aggradation rate is set at 25 m/Myr for the reference cases but we also present a set of wide-margin models with aggradation rates of 10 and 100 m/Myr which result in very thin and very thick pre-salt, respectively. Salt aggradation occurs at 2 km/Myr below −750 m of sea-level during the last 1–2 Myr of rifting. Salt is thus deposited rapidly after the bulk of crustal extension has ceased, immediately prior to continental break-up and development of oceanic crust forming a contiguous basin across both conjugates (Figure 3). The timing of salt deposition and consequently the thickness of the pre-salt syn-rift succession varies for each model as models with stronger crust breakup earlier than those with weaker crust (Figure 3). Post-rift dynamic progradation occurs below −250 m of base-level with a constant sediment flux of 0.001 m^3/s (~30 km^3/Myr) for all models. This is consistent with post-rift sediment fluxes (0.3–52 km^3/Myr) along the South Atlantic African margins (Baby et al., 2020).

The salt is treated as a linear viscous material with a viscosity of 5×10^{18} Pa s for the main set of models. End-member viscosities of 10^{18} and 10^{19} Pa s are also tested and presented in Figure S2.1 of Supporting Information S1. The viscosity values used in our study cover the range of viscosities expected for salt successions with distinct compositions and small (<10%) proportions of interbedded non-halite lithologies, including anhydrates, carbonates, potassium salts (C. A. L. Jackson, Jackson, Hudec, & Rodriguez, 2015; Rodriguez et al., 2018; Rowan et al., 2019). A linear (Newtonian) viscous salt rheology is a valid approximation based on laboratory experiments of halite deformation by pressure solution (Carter et al., 1993; Spiers et al., 1990; Van Keken et al., 1993), which has been widely used in numerical modeling studies (Albertz & Ings, 2012; Allen & Beaumont, 2016; Gemmer et al., 2004; Goteti et al., 2013; Gradmann & Beaumont, 2017). For simplicity, we focus on presenting and discussing only the left margin of each model as the width and geometry of their conjugates and the overall style of salt tectonics are similar (see Supporting Information S1). The final stages of the conjugate right margins are nonetheless presented in Figure S2.2 of Supporting Information S1 and Movies S8–11. The design parameters are outlined in Table 1 and the initial configuration of the salt basins (i.e., prior to continental breakup and at the onset of post-salt sedimentation) for each crustal type is shown in Figure 3.

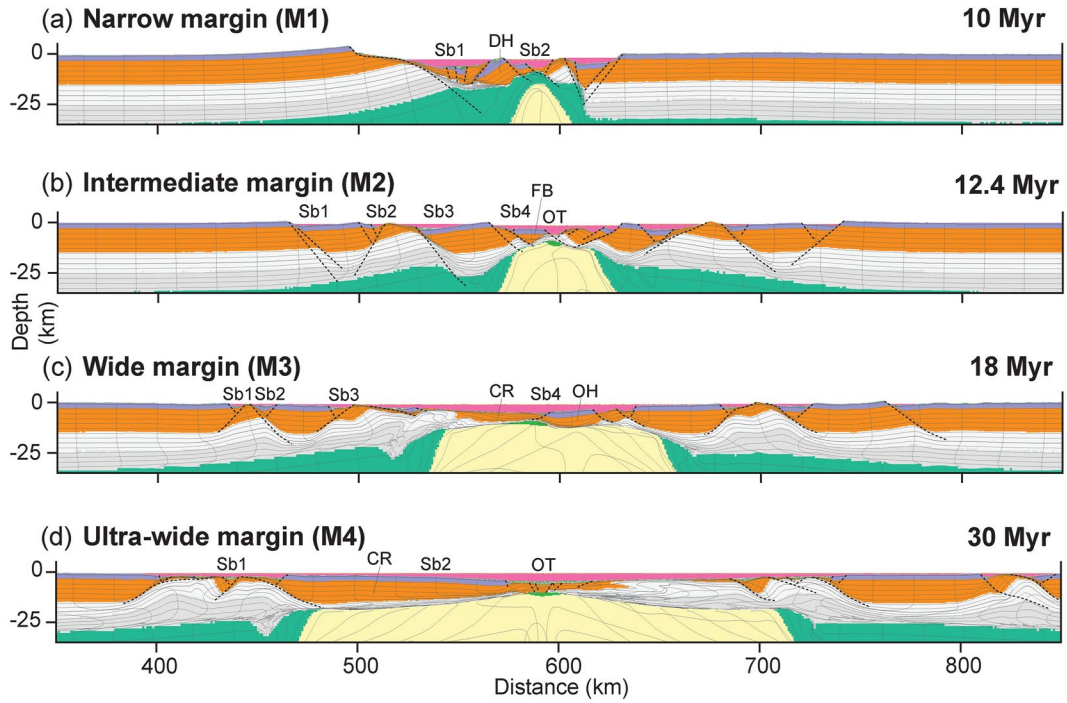

Figure 3. Snapshot showing the end of salt (pink) deposition for models (a) M1, (b) M2, (c) M3, and (d) M4. Salt is deposited 1–2 Myr prior to continental breakup and forms a contiguous salt basin along the two conjugates. Salt basin geometry, width and thickness varies according to the crustal strength and margin type. Sb, sub-basin; DH, distal high; FB, fault block; OT, outer trough; and CR, crustal raft. Syn-rift faults are in black dashed lines.

3. Results

3.1. Narrow Margin (Model M1)

Model M1 with a strong crustal rheology, produces narrow and asymmetric rifted margins (Figure 3a). Continental breakup is achieved at ~10 Myr, immediately after the end of salt deposition (Movie S1, supplementary material). The left, wider margin is characterized by a large seaward-dipping normal fault that cuts the entire crust and upper mantle (Figures 3a and 4a). Secondary normal faults dipping both land- and seaward define a series of internal highs and asymmetric grabens that are filled with syn-rift sediments up to 1–1.5 km thick, whereas little to no sediments are deposited on structural highs (Figure 4a). A piece of mid upper-crust occurs adjacent to the distal high (DH) and is formed by rift-flank collapse and gravitational instability of the steep rift flank (see Movie S1, 4.4 and 4.6 Myr). The distal margin comprises a set of seaward-dipping normal faults and rotated fault-blocks and a distal high with ~1 km of relief separating the salt basin into two disconnected sub-basins (Sb1 and Sb2, Figures 3a and 4). The proximal salt sub-basin (Sb1) is ~45 km wide with up to 3.2 km thick salt. The distal sub-basin (Sb2) is initially ~25 km wide with up to 3.8 km of salt (Figure 4a), but it is stretched and split into two soon after salt deposition as the conjugate margins become fully separated and oceanic crust develops (Figure 4a, Movie S1). The proximal salt is deposited when the underlying faults are inactive (Sb1), whereas the distal salt (Sb2) forms during latest syn-rift extension and shows syn-depositional thickening (Figure 4a, Movie S1).

At 15 Myr, salt deformation within Sb1 is characterized by seaward salt evacuation from underneath the prograding upper slope, salt inflation and diapirism at the toe of the slope and against the distal high (DH, Figure 4a). A series of 3–4 km tall, upright diapirs (2–5) and a salt anticline form above the inflated salt that are surrounded by symmetric, bowl-shaped minibasins with vertically aligned depocentres (Figure 4a). A minor (<1 km) minibasin forms above diapir 4 splitting it into two narrower diapirs, 4a and 4b (Figure 4a, Movie S1). Distal sub-basin 2 (Sb2) exhibits a diapir bounded by a proximal expulsion rollover (6) and two broadly upright diapirs (7–8) at the transition to a ~15 km wide salt nappe overlying the oceanic crust (Figure 4a). This nappe presents a set of small (~1 km) tall salt anticlines and is emplaced above exhumed mantle and oceanic crust soon after salt deposition, during the earliest stage of oceanic spreading (Figure 4a, Movie S1). No salt was originally deposited on top of oceanic crust.

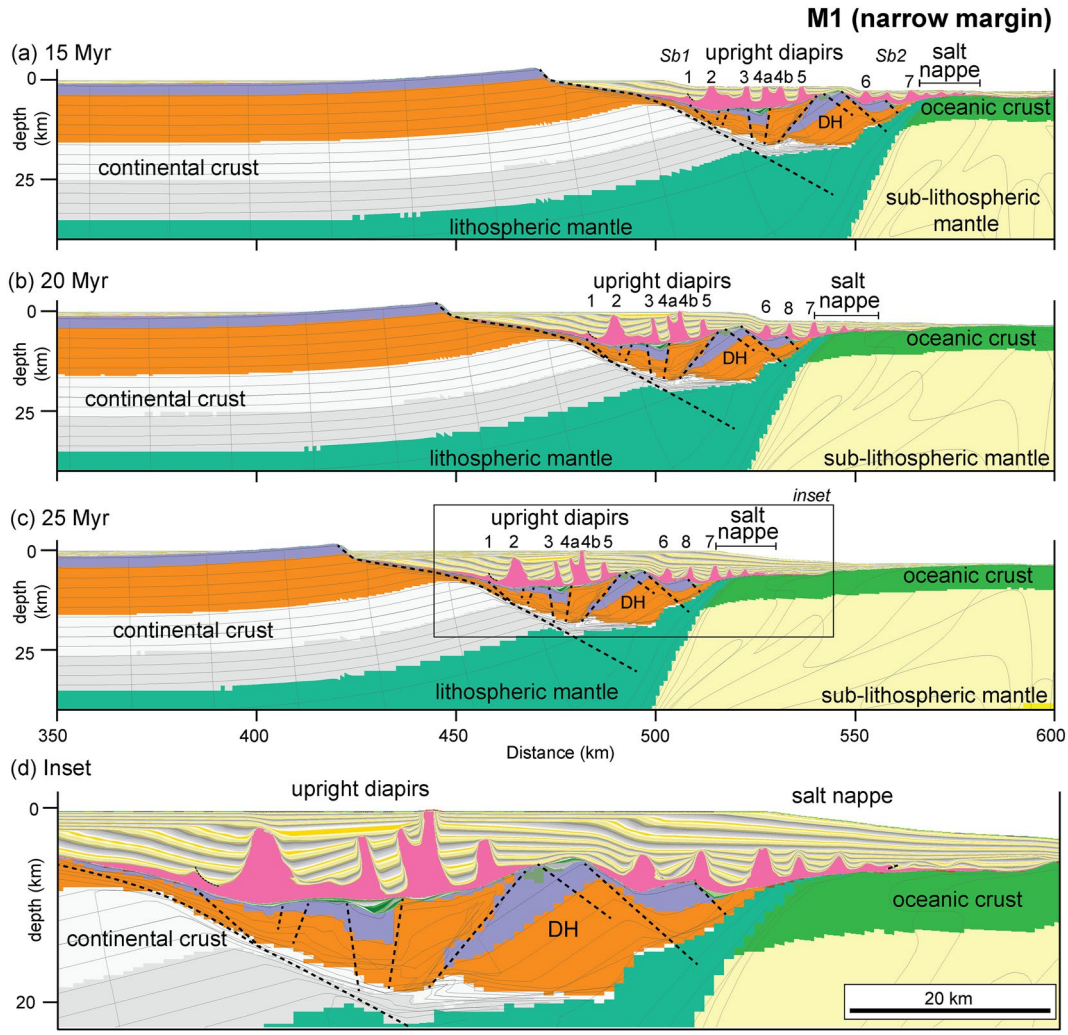

Figure 4. Snapshots of the narrow margin model M1 showing model evolution at (a) 15, (b) 20, and (c) 25 Myr of model run (see also Movie S1). Black box refers to the inset displayed in (d). Sb, sub-basin and DH, distal high. Syn- and post-rift normal faults in black dashed lines. Numbering refers to individual diapirs. The margin is characterized by two isolated salt sub-basins with dominantly vertical salt tectonics, upright diapirs and symmetric, simple minibasins and a ~24 km wide salt nappe with more limited diapirism over oceanic crust.

At 20 Myr, most salt structures are amplified as post-rift sediment progradation continues (Figure 4b). Proximal diapirs 2 to 4 rise further, reaching up to 5 km height. Their surrounding minibasins thicken and rotate landward as both salt and overburden translate ~2.5 km seaward over small base-salt steps until being buttressed against the distal high (Figure 4b). All salt structures in the distal sub-basin (Sb2) become narrower and taller, with anticlines evolving into diapirs (6–8, Figure 4b). There is no additional translation of the salt nappe as most of its salt is evacuated into diapirs (Figures 4a and 4b). At 25 Myr, there is little additional salt deformation apart from diapir 4b that rises and reaches the seafloor (Figures 4c and 4d).

3.2. Intermediate Margin (Model M2)

Model M2 with intermediate-strength crust results in 130–140 km wide symmetric conjugate margins (Figure 3b). Breakup is achieved at 12.5 Myr, immediately after the end of salt deposition. The left-margin is characterized by four 5–30 km wide half-grabens with predominantly seaward-dipping normal faults that cut the upper crust and detach in the weak mid-lower crust (Figures 3b and 5a). Faults and syn-rift fill are progressively younger seaward so that distal graben has little pre-salt syn-rift sediments (Figures 3b and 5a). The syn-rift grabens control the geometry, width, and thickness of the overlying salt sub-basins (Sb1-4), with thickest (up to 4 km) salt in their hangingwalls

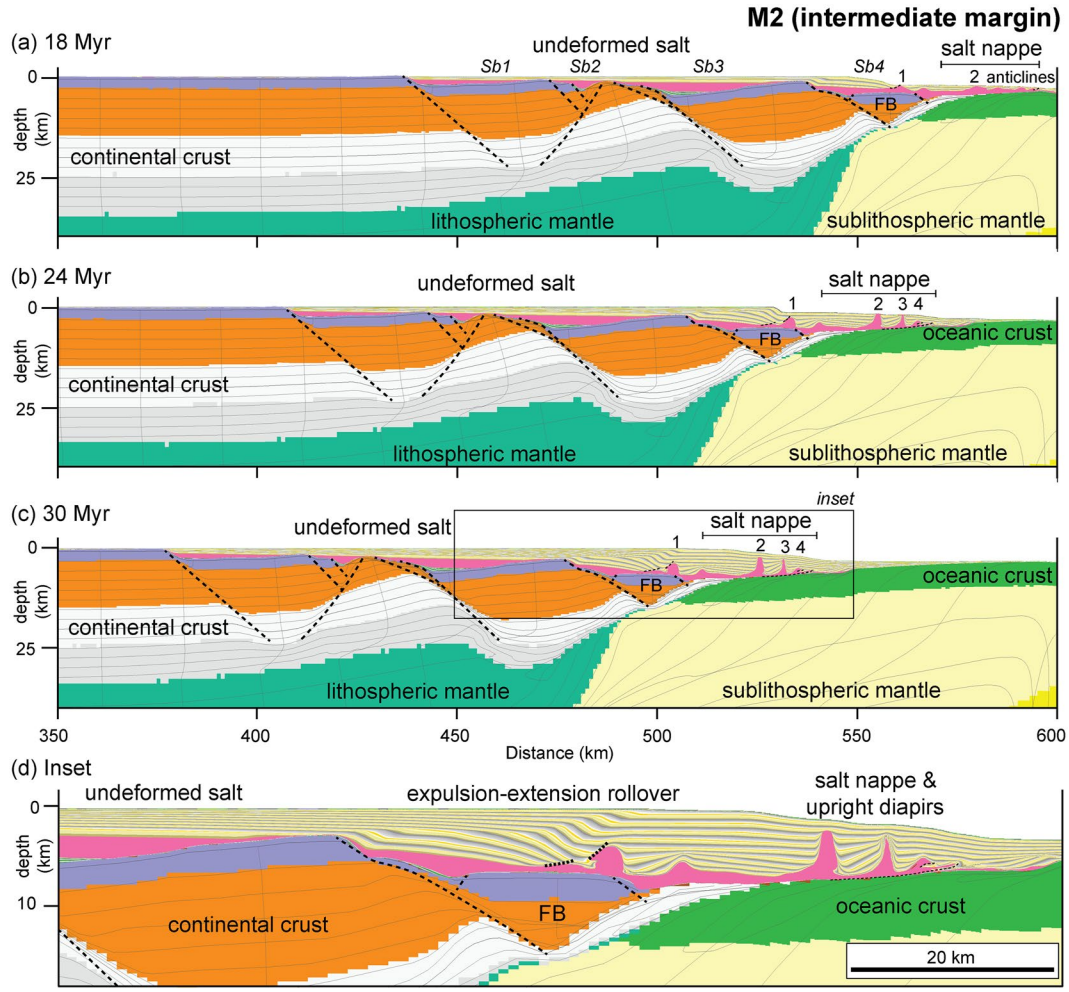

Figure 5. Snapshots of the intermediate-width margin model M2 showing model evolution at (a) 18, (b) 24, and (c) 30 Myr of model run (see also Movie S2). Black box refers to the inset displayed in (d). Sb, sub-basins; and FB, distal fault block. Syn- and post-rift normal faults in black dashed lines. Numbering refers to individual diapirs. The margin is characterized by four, largely isolated salt sub-basins, the most proximal of which are largely undeformed. Salt deformation is localized over the transitional and distal domain with development of a large, basinward-dipping expulsion rollover associated with limited (~5 km) of extension along landward-dipping normal faults. A ~28 km salt nappe overlies exhumed lower crust and oceanic crust with development of broadly upright diapirs and wedge-shaped minibasins.

pinching out toward their footwall highs (Figure 3a). The two proximal grabens present ~5–20 km wide and disconnected sub-basins 1 and 2, ~0.6 and 1 km thick, respectively. Intermediate sub-basin 3 is ~34 km wide, with maximum 1.6 km salt thickness (Figure 3a). Salt thickness in distal sub-basin 4 varies between 1.5 and 4 km with most salt deposited in the outer trough (OT). The initially thickest salt in the outer trough is thinned and stretched directly after its deposition as the two conjugate margins and their respective salt basins separate (Figure 5a, Movie S2).

At 18 Myr, proximal sub-basins 1 to 3 are rapidly buried by prograding sediments and largely undeformed (Figure 5a). Salt deformation is focused on sub-basin 4 with salt expulsion from underneath the prograding upper slope forming a small seaward-dipping rollover bounded by a ~1 km tall triangular diapir (1) at the edge of the distal fault-block. An asymmetric, landward-thickening minibasin and a ~1.5 km tall salt anticline form further seaward (Figure 5a). At the transition between lower continental crust and oceanic crust, a broad (~5 km wide and 2 km tall) diapir (2) forms above a ~24 km wide allochthonous salt nappe. Above the oceanic crust, the nappe is associated with low amplitude (<1 km) salt anticlines and a small thrust at its toe (Figure 5a).

At 24 Myr, continued progradation produces amplification of the seaward-dipping rollover associated with inflation and ~4 km of translation of bounding diapir 1 (Figure 5b). The adjacent minibasin and salt anticline translate

~4 km seaward onto the exhumed lower crust (Figure 5b). Seaward, ~4 km of salt advance over oceanic crust and the most distal post-salt sediments results in a ~28 km wide salt nappe (Figure 5b). The nappe develops ~4 km tall diapirs (2–4) surrounded by asymmetric minibasins with upturned near-diapir strata (Figure 5b). At 30 Myr, there is little additional salt deformation and/or overburden translation as most of the salt has already been evacuated into salt structures and is buried by the gradually thickening overburden apart from limited (~0.5–1 km) rise of the two largest diapirs (2–3) (Figures 5c and 5d).

3.3. Wide Margin (Model M3)

Model M3 has a weak crustal rheology that results in early rupture of the mantle lithosphere at ~9 Myr and breakup of the continental crust at ~18 Myr forming ~200 km wide conjugate margins (Figure 3c, Movie S3). The left-margin is defined by three symmetric horsts and grabens in the proximal domain (Figure 3c) and passes seaward into a half-graben bounded by a low-angle seaward-dipping fault and a ~60 km wide, highly thinned crustal raft with distributed deformation. The distal margin exhibits a ~20 km wide outer high adjacent to the early oceanic crust (OH, Figures 3c and 6).

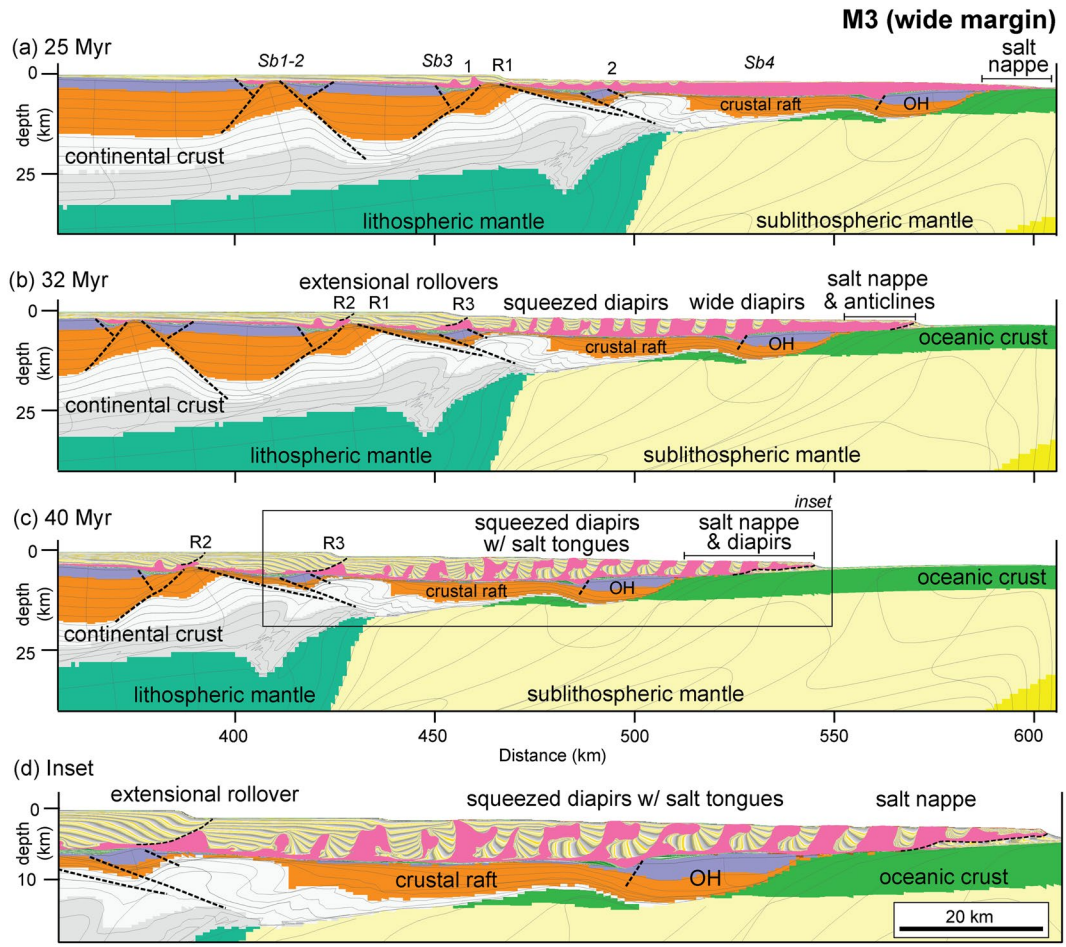

Figure 6. Snapshots of the wide margin model M3 showing model evolution at (a) 25, (b) 32, and (c) 40 Myr of model run (see also Movie S3). Black box refers to the inset displayed in (d). Sb, sub-basins; OH, outer high. Syn- and post-rift normal faults in black dashed lines. The numbering refers to individual diapirs, R1-3 refers to extensional salt rollers and rollovers formed in the proximal domain characterized by salt-detached updip extension. The margin is characterized by two salt sub-basins that are connected over subtle base-salt relief and form a ~200 km wide salt basin. The basin displays significant (~20 km) updip extension associated with counter-regional normal faults and rollovers, intermediate translation and multiphase, complex diapirs and minibasins and downdip diapir shortening. A ~36 km wide salt nappe develops at the distal edge of the basin and is associated with broad near-surface diapirs and wedge-shaped minibasins.

All grabens are filled by 0.5–1 km thick pre-salt syn-rift sediments, with thinner pre-salt sediments on the structural highs. The salt forms a ~180 km wide largely continuous salt basin that gradually thickens seaward, reaching ~4 km in its deepest portion (Figure 3c). The two proximal grabens form 10–14 km wide semi-isolated salt sub-basins (Sb1 and (b) with up to ~1 km thick salt. Sub-basin 3 is ~36 km wide with up to 1.2 km thick salt in its deepest portion (Figure 3c). Sub-basin 4 is ~170 km wide and forms over the crustal raft and outer high and connects the two conjugate margins before breakup. This sub-basin is subsequently split into two as the two conjugate margins become separated during continental breakup and oceanic spreading (Figure 6a, Movie S3). Subtle (~0.5 km) salt thickness variations are observed within individual sub-basins over rift-related base-salt relief.

At 25 Myr, lithosphere breakup has separated the conjugate margins with distal sub-basin 4 that is ~120 km wide and with a ~16 km wide salt nappe on top of early oceanic crust on the left conjugate margin (Figure 6a). Proximal sub-basins 1 and 2 exhibit minor salt inflation and development of <0.5 km high salt anticlines (Figure 6a). Sub-basin 3 contains 1.5–2 km tall diapirs surrounded by symmetric minibasins (1, Figure 6a). A seaward-dipping expulsion rollover (R1) forms in the transition to sub-basin 4 beneath the prograding upper slope. Further seaward, the salt is inflated and develops anticlines and ~1.5 km high diapirs (2) associated with symmetric minibasins underneath the lower slope (Figure 6a). There is limited salt deformation further seaward apart from subtle folding at the toe of the nappe (Figure 6a).

At 32 Myr, sub-basins 1 and 2 are covered by prograding sediments and stop deforming. Sub-basin 3 shows minor growth of both diapirs (Figure 6b). Diapir 1 develops a landward-dipping normal fault with a seaward-dipping rollover in its hangingwall (R2, Figure 6b). Rollover R1 is inactive at this stage. Further seaward, rollover R3 forms above the previously inflated salt, bound by a landward-dipping normal fault and a triangular diapir (Figure 6b). Seaward, sub-basin 4 develops a series of inclined and squeezed, 3–4 km tall teardrop diapirs associated with highly upturned to overturned near-diapir strata within asymmetric, slightly rotated minibasins. Simpler, wide diapirs with broadly upright minibasins occur further seaward (Figure 6b). Most of these diapirs reach the seafloor. The distal salt nappe advances a further ~4 km over the oceanic crust, reaching a width of ~20 km (Figure 6b).

At 40 Myr, proximal rollovers R2 and R3 are amplified associated with translation of the underlying salt, accommodating respectively ~6 and 12 km of extension along their landward-dipping normal faults (Figure 6d, Movie S3). Over the crustal raft, the proximal diapirs become inactive and buried by prograding sediments whereas the distal ones are squeezed and continue to rise, developing complex geometries (Figures 6c and 6d). Wider and relatively more symmetric, 3–4 km tall diapirs form further seaward, over the distal salt nappe, with simpler bowl- and wedge-shaped minibasins (Figures 6c and 6d). The nappe reaches a total width of ~32 km (Figure 6c, Movie S3).

3.4. Ultra-Wide Margin (Model M4)

Model M4 has a very-weak crustal rheology in which the upper crust and upper mantle-lithosphere are fully decoupled leading to distributed upper crustal extension and formation of two ~300 km wide conjugate margins characterized by high-offset, low-angle faults and pronounced middle-lower crustal flow (Figure 3d). Continental breakup is achieved at ~31 Myr, soon after salt deposition (Figure 3d, Movie S4). The left-margin is characterized by a ~75 km wide proximal graben, a ~110 km wide crustal raft, and a ~20 km wide highly thinned outer through (Figure 3d). A ~400 km wide, broadly continuous salt basin forms across the conjugate margins (Figure 3d), which are later split into two with continental breakup and oceanic spreading. In the left-margin, sub-basin 1 is ~70 km wide and filled by 1–1.5 km thick pre-salt sediments and ~1.5 km thick salt (Figures 7a–7e). The crustal raft shows distributed syn-rift deformation, <300 m thick pre-salt sediments, and ~130 km wide salt that thickens gradually seaward. The outer trough accommodates up to 1.5 km thick pre-salt sediments and up to ~4 km of salt that exhibits syn-depositional thickening associated with ongoing rifting (Figure 3d, Movie S4). The outer trough evolves into a structural high after the onset of oceanic spreading and upwelling of the sub-lithospheric mantle (Figure 7).

At 50 Myr, post-rift sediment progradation over salt sub-basins 1 and 2 is associated with salt deformation characterized by <1 km tall salt anticlines, 3–4 km tall diapirs with complex geometries, and asymmetric wedge-shaped minibasins (Figures 7a and 7d). Above the crustal raft updip portion, salt tectonics is characterized by anticlines and small (1.5–2 km) diapirs whereas the outer through shows no visible salt deformation at this stage (Figure 7a). Salt has advanced ~32 km over the early oceanic crust associated with late syn-rift salt stretching (Movie S4). This allochthonous salt is largely undeformed apart from its most distal part (Figure 7a).

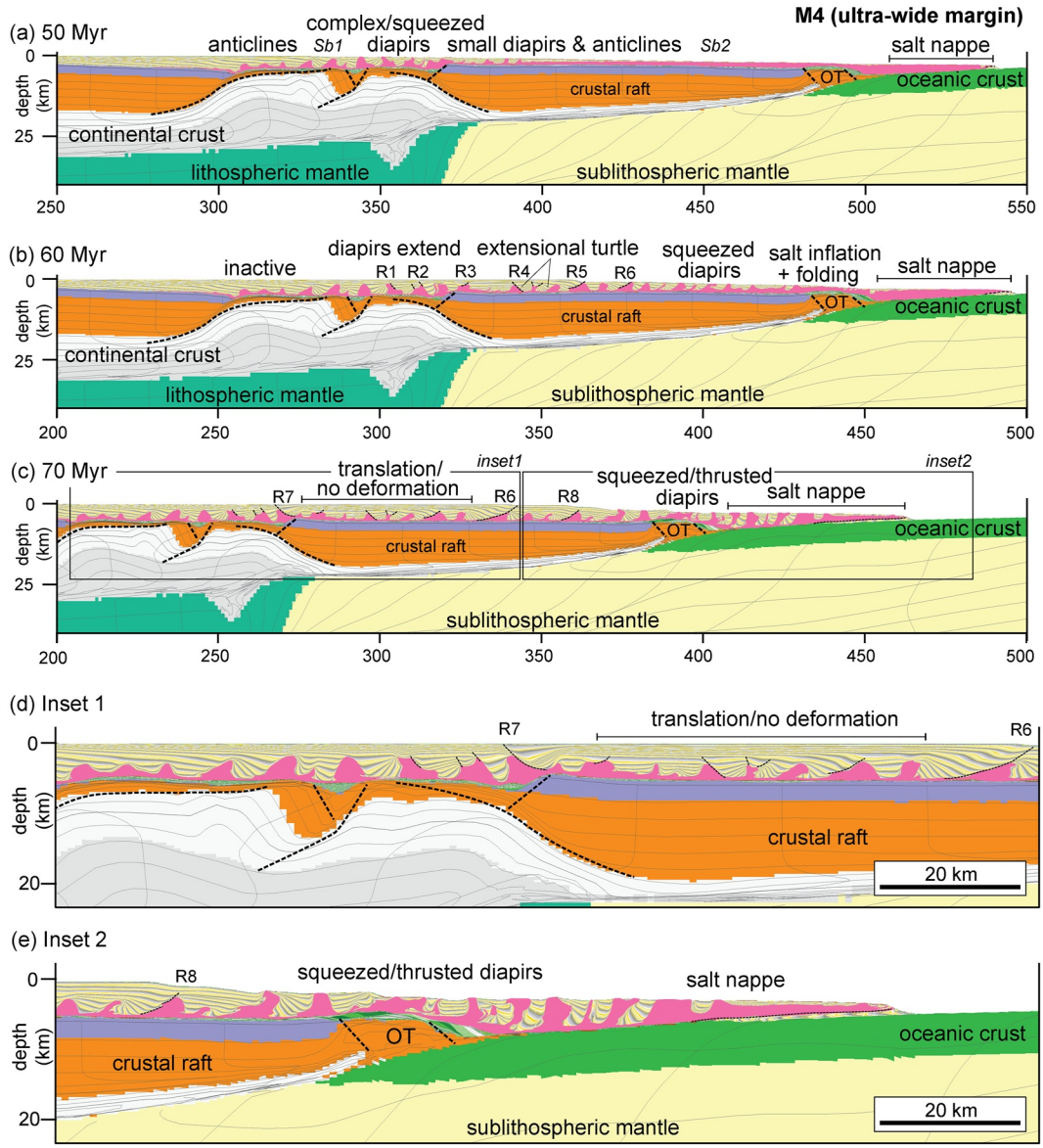

Figure 7. Snapshots of the ultra-wide margin model M4 showing model evolution at (a) 50, (b) 60, and (c) 70 Myr of model run (see also Movie S4). Black boxes refer to the insets (d) 1 and (e) 2. Sb, sub-basins; OT, outer through, which is later inverted to form a high. Syn- and post-rift normal faults in black dashed lines. R1-6 refers to rollovers formed in the proximal to transitional domains. The margin presents a ~250 km wide salt basin with limited base-salt relief and significant salt connectivity across subtle base-salt relief. Proximal deformation is dominated by complex, multiphase diapirism and wedge-shaped minibasins over a partially isolated proximal sub-basin. Further downdip, there is pronounced (~30 km) extension associated with normal faults, rollovers and turtle anticlines, intermediate translation of salt and overburden, complex diapirism and downdip shortening. A ~56 km wide salt nappe occurs at the distal edge of the basin overlying the oceanic crust and demonstrating significant, complex diapirism and minibasin development.

At 60 Myr, the most proximal salt structures become inactive as they are covered by prograding sediments. The distal half of sub-basin 1 shows significant salt deformation with ~4 km of extension along seaward-dipping normal faults and development of rollovers (R1 and R2) at the crest of earlier diapirs (Figure 7b and inset on Figure 7d). Previously inflated salt at the distal edge of sub-basin 1 translates over the crustal raft, developing a landward-dipping normal fault and an extensional rollover (R3, Figures 7b and 7d). Further seaward, 2–3 km tall diapirs form over the crustal raft associated with seaward- and landward-dipping rollovers R4-6, symmetric and asymmetric rotated minibasins, salt tongues, and turtle structures (Figures 7b and 7d). At the distal portion of the crustal raft and outer-through, salt deformation is characterized by salt inflation, anticlines, and few 1–2 km tall

seaward inclined squeezed diapirs (Figure 7b). The allochthonous salt nappe inflates and advances further ~8 km over the oceanic crust and distal post-salt sediments (Figure 7b, Movie S4).

At 70 Myr, proximal sub-basin 1 is inactive as it is covered by >6 km thick sediments. A new seaward-dipping normal fault and extensional rollover forms at the distal edge of sub-basin 1 (R7; Figure 7d). The salt and overburden translate ~5 km seaward in the updip portion of crustal raft in sub-basin 2 without significant additional deformation (i.e., rollovers R1–R5 become inactive, Figure 7d, Movie S4). Landward-dipping normal faults and 3–4 km thick rollovers R6 and R8 form on top of earlier diapirs and minibasins over the downdip portion of the crustal raft (Figure 7d). As salt and overburden translate ~14 km seaward over the crustal raft, the diapirs located in the distal end of the basin are squeezed and thrusted over their adjacent minibasins and transported beyond the outer through (Figure 7d). Squeezed, seaward-leaning diapirs with rotated minibasins form in the updip portion of the salt nappe, which translates an additional ~14 km seaward over post-salt sediments, reaching a width of ~54 km and developing small diapirs and anticlines at its toe (Figures 7c–7e, Movie S4).

3.5. Sensitivity to Pre-Salt Syn-Rift Thickness

We next assess the role of variable pre-salt syn-rift sediment thickness on salt basin geometry and salt tectonics using the wide-margin model as reference. We compare the final stages of deformation for models with two end-members syn-rift sedimentation rate: model M5 with a very low rate of 10 m/Myr and model M6 with a very high rate of 100 m/Myr. The models exhibit a decrease in salt thickness and base-salt relief with increasing pre-salt sediment thickness and a consequent decrease in the number of diapirs and structural complexity (Figure 8). We note that the rifted margin architecture and fault geometries of these two models differ slightly between each other and reference model M3 owing to the feedback between syn-rift sedimentation and rifting (cf., Andrés-Martínez et al., 2019; Theunissen & Huismans, 2019; Wolf et al., 2022).

In model M5, with very thin pre-salt and thicker salt (Figure 8a), four counter-regional, that is, landward-dipping normal faults and associated extensional rollovers and diapirs form above Sb3 and the updip portion of Sb4. In M6, with very thick pre-salt and thin salt (Figure 8b), there is negligible salt deformation and diapirism in Sb3. Three extensional rollovers overlying either landward- or seaward-dipping normal faults form in M6, but these

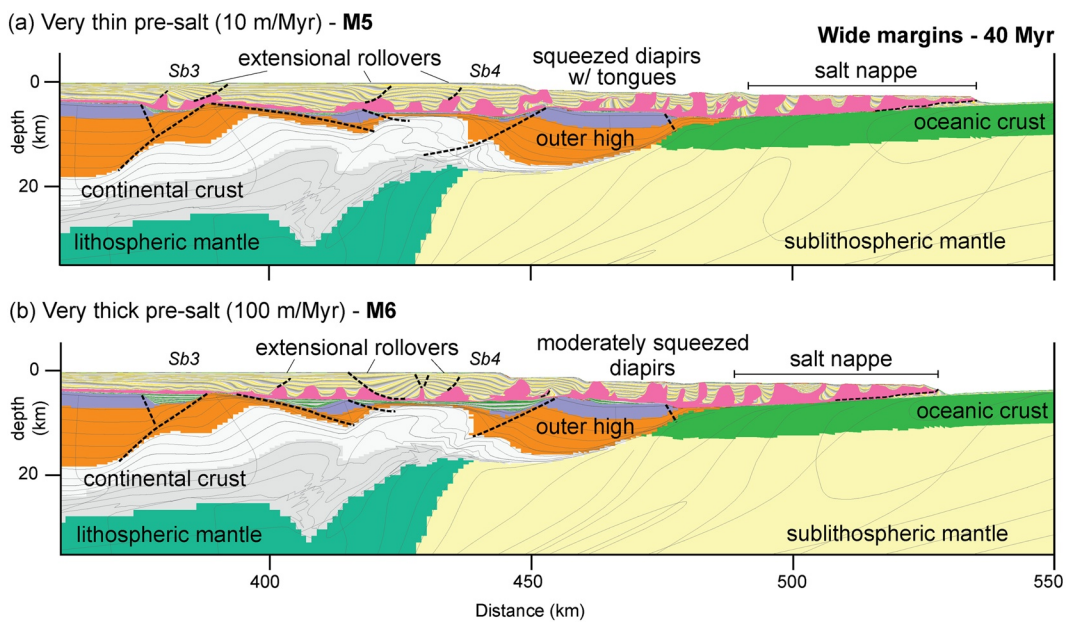

Figure 8. Comparison of the magnitude and style of salt tectonics at the final stage (40 Myr) between wide margin models (a) M5 and (b) M6 having different end-member pre-salt syn-rift thicknesses. See also Movies S5 and S6. Faults in black dashed lines. For additional models showing variations between pre-salt and salt thickness according to the rate of pre-salt syn-rift aggradation see supplementary material. Very thick pre-salt sediments (M6) produce thinner salt and a simpler style of deformation, with overall less diapirism and structural complexity than the very thin pre-salt model (M5). The magnitude of updip extension, downdip diapir shortening and nappe advance are also smaller for very thick pre-salt.

occur further seaward, within Sb4, relative to M5. In both models, the magnitude of updip extension is broadly similar, ~16 km for M5 and ~18 km for M6. Further seaward, over the outer high in the distal margin, there is significantly greater complexity in the model with very thin pre-salt, M5, compared to M6 with very thick pre-salt. M5 develops six, variably-shaped diapirs, most of which are significantly squeezed, with salt tongues and more complex minibasin geometries, whereas M6 presents only four, moderately squeezed diapirs with simpler salt and minibasin geometries. The distal salt nappe varies in width from ~45 km in M5 to ~40 km in M6 but with similar overlying diapir and minibasin geometries. We note these nappes are slightly wider than in the reference model, M3, due to the slightly narrower (<10 km) continental crust domain (Figures 6 and 8).

3.6. Sensitivity to Post-Salt Relative Progradation Rate (V_{prog}/W)

We next assess the role of variable post-salt sedimentation rate on rifted margin salt tectonics in terms of progradation rate (V_{prog}) relative to margin and salt basin widths (W). We compare the narrow margin model M1, that has a ~100 km wide margin and the reference sediment flux (30 km^3/Myr) and average progradation rate of 2.4 mm/year (Figure 9a) with the wide margin model M7, that is ~200 km wide and has double the sediment flux (60 km^3/Myr) and progradation rate (4.8 mm/year) (Figure 9b), relative to the reference wide margin model M3 (Figure 9c). Models M1 and M7, thus have the same ratio between post-rift sediment progradation rate and margin width. As M1 and M7 are covered by prograding sediments within the same time frame they allow us to examine how other factors including differences in base salt relief and salt volume affect salt tectonics on these contrasting margin types.

Both model M1 and M7 exhibit limited lateral salt tectonics (i.e., updip extension and downdip shortening) and diapirism, in comparison to the reference wide margin model, M3 (Figure 9). For wide margin model M7,

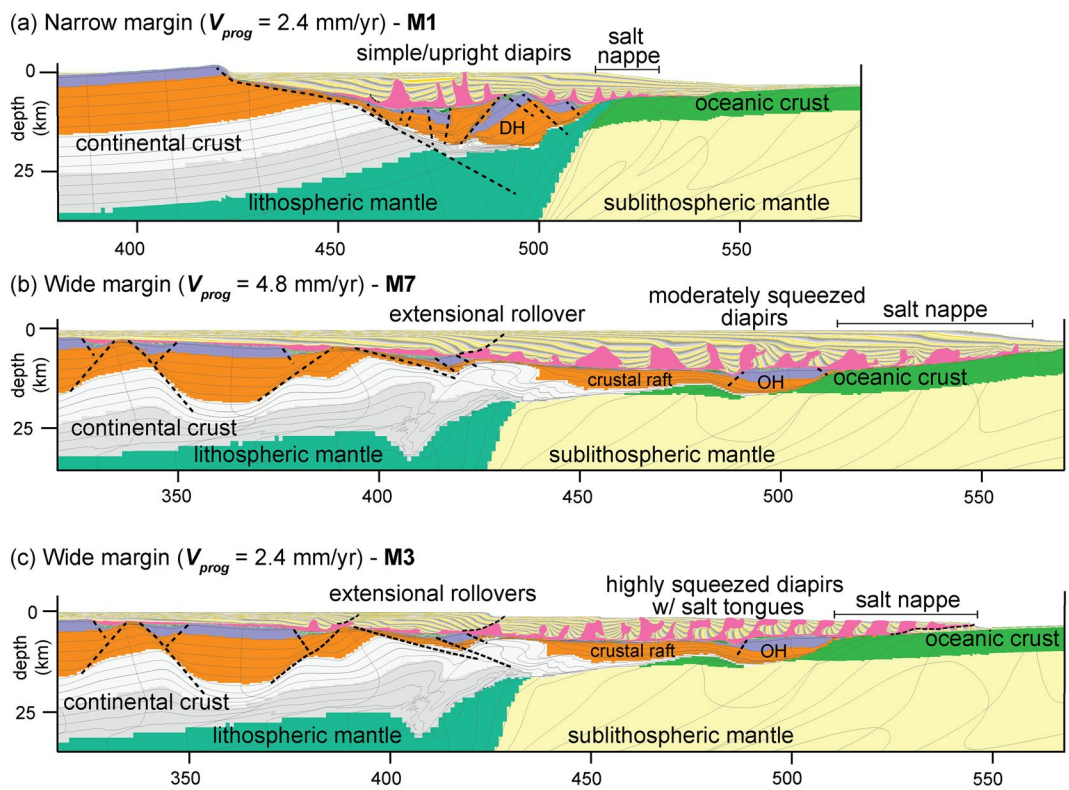

Figure 9. Comparison of the magnitude and style of salt tectonics at the final stage between (a) narrow (M1) and wide margins, (b) M7, and (c) M3 with different post-salt sediment progradation rates relative to margin width (V_p/W). (a) M1 has a ~100 km salt basin and the reference progradation rate V_{prog} = 2.4 mm/yr. (b) M7 has a ~200 km wide salt basin and a double the progradation rate V_{prog} = 4.8 mm/yr (see also Movie S7). Models in (a) M1 and (b) M7 have therefore the same relative rate of progradation. (c) M3 with the reference progradation rate V_{prog} = 2.4 mm/yr for comparison with the same margin type (M7) with different rates. Faults are in black dashed lines. DH, distal high; and OH, outer high.

doubling the progradation rate produces only ~11 km of updip extension compared to ~18 km for M3, whereas for narrow margin model M1, updip extension is only ~3 km (Figure 9). The overall salt tectonics architecture is also simpler in M7 compared to M3, characterized by fewer and more upright diapirs, less rotated and more symmetric minibasins, and a less deformed salt nappe, and somewhat similar to the narrow margin model M1. The magnitude of post-rift nappe advance, however, increases for increasing progradation rates for the same margin type, as for example, for the wide margins, it varies from ~16 km in M3 to ~28 km in model M7 (Figure 9). Doubling the progradation rate in M7 produces higher differential sediment loading and greater expulsion of the more proximal salt onto the distal margin and salt nappe.

3.7. Dynamic Analysis

We next analyze several key measures in the models including salt volume, relative progradation rate, base salt relief, metrics quantifying the structural style of salt tectonic deformation, and how they vary with margin width (Figure 10). Margin width is directly controlled by crustal strength (Theunissen & Huismans, 2019). Salt volume is proportional to margin width, with ultra-wide margins having approximately three times the volume

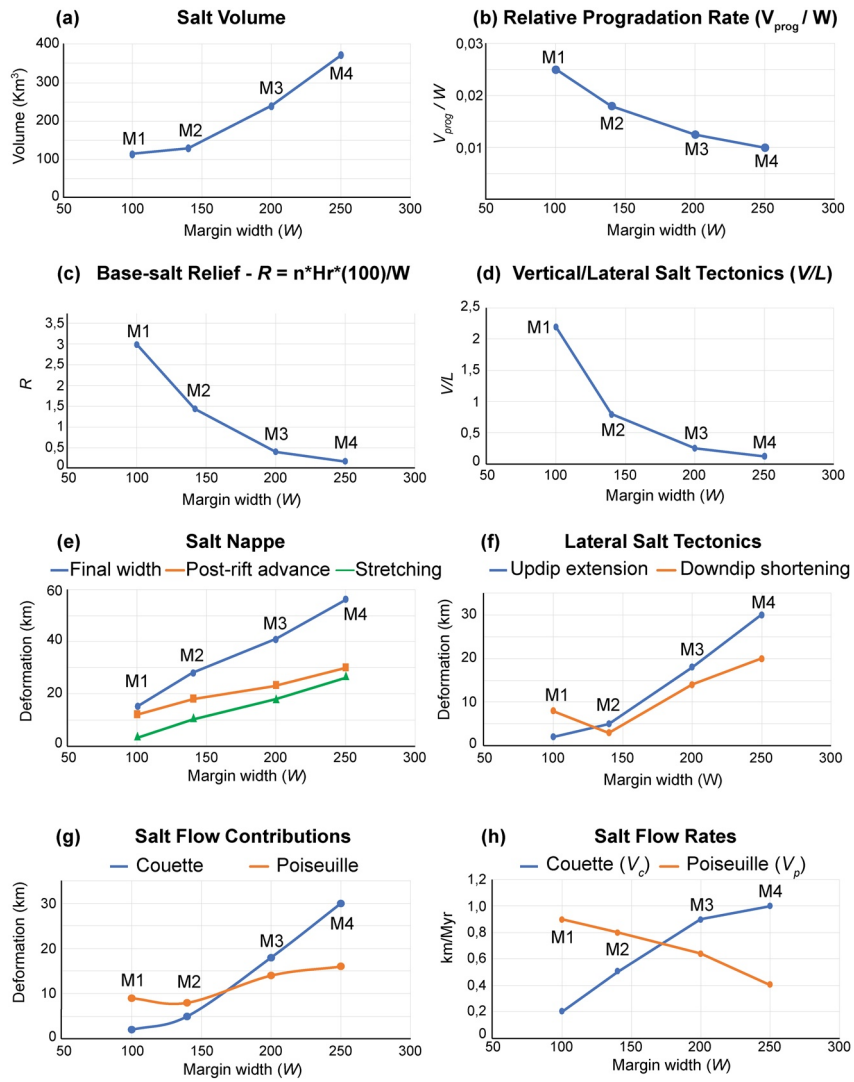

Figure 10. Quantitative dynamic analysis plots for the different margin types and widths: (a) salt volume, (b) relative progradation rate, (c) base-salt relief (*R*), (d) ratio between vertical and lateral salt tectonics (*V/L*), (e) salt nappe width, syn-rift stretching and post-rift advance, (f) lateral salt tectonics, updip extension and downdip shortening, (g) estimated Couette and Poiseuille salt flow contributions, and (h) Couette and Poiseuille flow average rates.

of narrow margin salt basins (Figure 10a). Post-rift sediment progradation rate, V_{prog}, is constant at 2.4 km/Myr, owing to a constant sediment flux for all models, but the relative rate of progradation decreases with margin width (Figure 10b). We define the non-dimensional base-salt structural relief, R, as the product of the number of base-salt highs, n, their average height, H_R, normalized by margin width, W:

$$R = (nH_R * 100) / W$$

Base salt relief is high for narrow margins and strongly decreases with margin width owing to the more distributed rifting and smaller offsets along individual normal faults for wider margins (Figure 10c). The ratio between lateral, downdip translation and vertical (i.e., diapiric rise) salt tectonics for the different margin types shows an inverse relationship between margin width and the ratio vertical/lateral salt tectonics (Figure 10d). Lateral salt tectonics corresponding to updip extension and downdip diapir shortening increases with margin width except for the intermediate margin case that shows lowest amount of downdip diapir shortening (Figure 10e). Total width of distal allochthonous salt on oceanic crust and contributions from syn-rift salt stretching and post-rift thrust advance also increase with margin width (Figure 10f). We lastly quantify the magnitude and average rate of Couette flow (V_c) (e.g., updip extension, overburden translation and downdip shortening) and the contribution of Poiseuille flow (V_p) (e.g., pressure-driven salt flow) to lateral salt tectonics (cf., Pichel et al., 2022). These values vary through time and space but are averaged over the entire post-rift (post-salt) model evolution. Poiseuille flow is inferred from the imbalance between salt nappe advance and overburden translation (cf., Pichel et al., 2022). Both magnitude and rate of Couette flow increase with increasing margin width (Figures 10g and 10h). The magnitude of Poiseuille flow similarly shows a general, although more subtle increase with increasing margin width, while the rate of Poiseuille flow decreases with increasing margin width.

4. Discussion

4.1. Styles and Controls of Salt Deformation Along Rifted Margins

The models presented here expand on Pichel et al. (2022) and show the interplay between syn-rift extension, late syn-rift salt deposition, post-rift sediment progradation, and salt tectonics for different rifted margin types and architectures. The degree and style of salt tectonics in the models presented here is controlled by the interplay of four main controlling factors: (a) the relative rate of post-rift sediment progradation vs. margin width, (b) salt volume, (c) base-salt relief, and (d) salt viscosity.

The relative rate of post-rift sediment progradation (V_{prog}) versus margin width (W), provides the first-order control on lateral salt flow. A low V_{prog}/W ratio promotes lateral salt flow resulting in prominent inclined and complex diapirs, asymmetric minibasins, and significant updip extension and downdip shortening, the latter in the form of diapir squeezing and buckle-folding. In contrast, high V_{prog}/W inhibits lateral flow resulting in predominantly upright diapirs, symmetric minibasins, and minor to absent updip extension and downdip contraction. The magnitude and variability of salt tectonics are also controlled by salt volume. Wider margins accumulate more salt leading to more evolved and greater diversity of salt structures. Base salt relief controls the continuity between the individual salt basins and the ability of the salt to behave as a single large weak layer below the prograding sediments, or as individual salt sub-basins. Consequently, base-salt relief also affects the ratio of horizontal and vertical salt tectonics. Low relief allows updip extension in the proximal to intermediate margin domains to link with downdip diapir shortening in the distal margin, as observed in wide and ultra-wide margin models with low base-salt relief. In contrast, high base-salt relief, characteristic for narrow to intermediate margin widths, disconnects the salt sub-basins and leads to salt structures restricted to the individual salt sub-basins. While not extensively investigated here we note that pre-salt sediment thickness modulates base salt relief and salt thickness (Figure 8, Supporting Information S1).

Lastly, salt viscosity and the ability for the salt to flow provide a first-order control on the degree and complexity of salt structures (supplementary models SM3a and SM3b, S2) (cf., Pichel et al., 2022). The general style and dynamics of salt deformation are broadly similar for different salt viscosities but differ in terms of magnitude of salt tectonic deformation, the final width of the nappe, and the size and complexity of diapirs (Pichel et al., 2022). The magnitude of extension, translation, shortening, and final width of the distal nappe increase with a decreasing salt viscosity. A decrease in salt viscosity is also associated with an increase in frequency and complexity of salt

tectonic structures and with a decrease in the height and width of salt diapirs. Thus, low salt viscosity promotes lateral flow and associated salt tectonic features and counteracts the effect of increasing the relative progradation rate. In contrast, high salt viscosity reduces or even inhibits lateral salt flow, even for relatively low progradation rates.

These four main controlling factors explain the contrasting salt tectonics in the models presented. Narrow margin model M1 exhibits high base-salt relief, a high relative progradation rate, and moderate to low salt volume. Salt tectonics in this case is dominated by vertical salt structures above the isolated individual salt sub-basins (Figure 11). In contrast, the ultra-wide margin model M4, with very subtle base-salt relief, a very low relative progradation rate, and high salt volume provides another end-member with regionally kinematically-linked lateral salt tectonics, significant updip extension balanced with downdip contraction, prominent inclined diapirs with rotated asymmetric minibasins, and a large allochthonous salt nappe on top of oceanic crust (Figure 11). Intermediate and wide margin models M2 and M3 exhibit behavior in-between these end member styles (Figure 11). The intermediate margin model M2 has, similarly to model M1, significant base-salt relief that reduces connectivity between the individual salt basins. In combination with the moderate salt volume, this results in limited margin-scale lateral salt tectonics. In contrast, the wide margin model M3 exhibits similar features as ultra-wide margin model M4 with connected salt sub-basins with low base-salt relief, high salt volume, and low relative progradation rate promoting kinematically-linked margin-scale lateral salt tectonics.

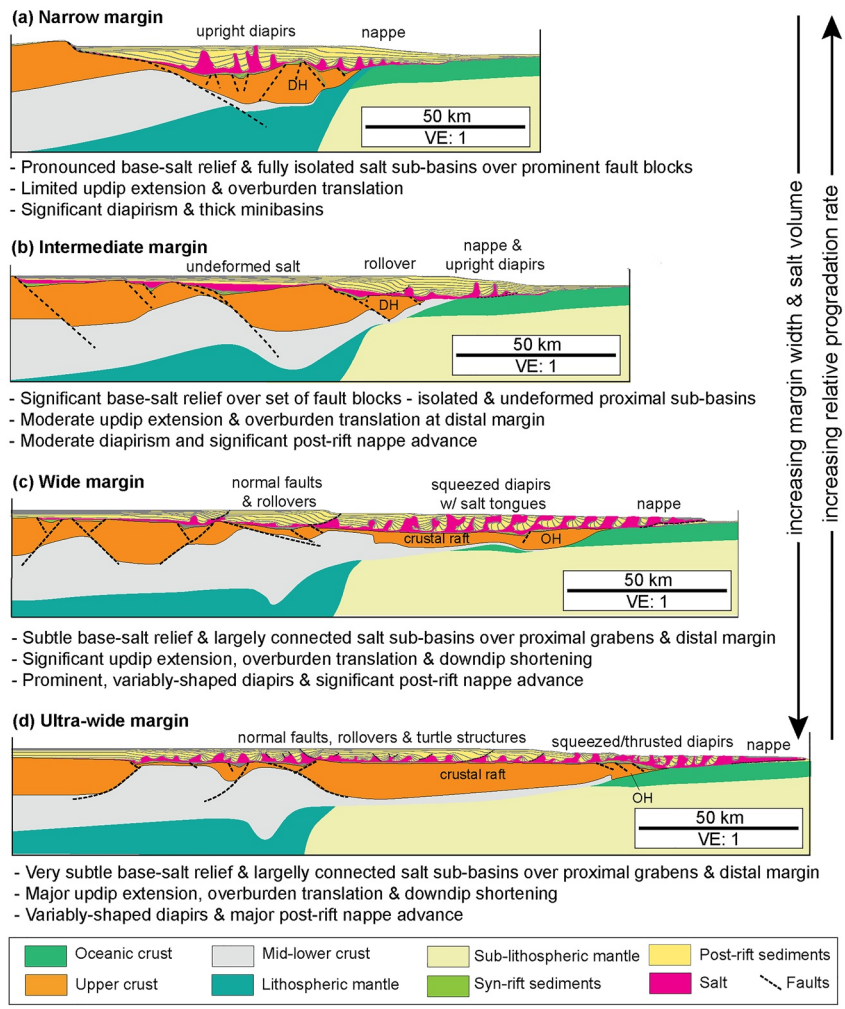

Figure 11. Synthesis diagram comparing the different styles and magnitude of salt tectonics according to the different margin types, rifted margin architecture and width based on the four main models of this study: (a) narrow (M1), (b) intermediate width (M2), (c) wide (M3), and (d) ultra-wide (M4) models. DH, distal high; and OH, outer-high.

As shown in Pichel et al. (2022) for wide rifted margins, our models demonstrate that the distal salt nappe overlying newly formed seafloor is a product of late syn-rift stretching and post-rift gravity-driven tectonics for all different margin types (Figures 4–7). The post-rift nappe advance is primarily controlled by pressure-driven Poiseuille flow whereas gravity-driven updip extension and downdip diapir shortening are controlled by Couette flow (Figure 10). Apart from M1, in all other models, the salt nappe is emplaced over newly formed oceanic crust. However, the distal salt nappe can equally advance over other newly-formed seafloor, such as exhumed mantle in magma-poor or SDRs in magma-rich margins (not modeled in this study).

4.2. Comparison With Natural Examples

Our model results are comparable to various natural systems, in particular to salt basins in the central South Atlantic, the Gulf of Mexico, the Red Sea, and parts of the Newfoundland-Nova Scotia and Morocco margins. Salt along these margins is deposited during the last stage of rifting, prior to continental breakup as in our models (Figures 1 and 3). Most salt tectonic deformation occurs in the first ∼0–60 Myr of their post-rift evolution and is associated with deposition of, on average, a ∼6–8 km thick prograding sedimentary succession (Figure 1) (Davison et al., 2012; Hudec & Jackson, 2004; Kukla et al., 2018; Peel, 2014; Rowan, 2020).

The style of salt tectonics, margin width, and architecture of narrow margin model M1 is comparable to segments of the northern Red Sea (Mohriak & Leroy, 2013; Rowan, 2014) and south Nova Scotia (Figures 1d and 1e). These margins are ∼80–100 km wide, with salt tectonics that exhibit limited updip extension (<5 km) and predominantly vertical salt tectonics with ∼3–5 km tall upright diapirs, and ∼10–20 km of salt nappe advance over transitional and/or oceanic crust (Figures 1d and 1e).

The style and magnitude of salt tectonics, margin width and architecture of model M2 can be compared with the Espirito Santo Basin, Brazil (Figure 1a) (Blaich et al., 2011; Kukla et al., 2018), parts of the northeast and the southern Gulf of Mexico (Hudec & Norton, 2019; Izquierdo-Llavall et al., 2022), Nova Scotia (Deptuck & Kendell, 2017) and northwest Africa (Tari et al., 2003, 2012, 2017). The Espirito Santo margin, for example, is ∼160 km wide, shows minor to no diapirism in the proximal domain, and a greater magnitude of updip extension along salt-detached normal faults (∼10 km) than narrow margins (cf., Figures 1d and 1e). Salt deformation in the transitional to distal domain exhibits broadly upright diapirs, slightly asymmetric minibasins, and a ∼15 km wide salt nappe, comparable to our intermediate margin model M2. We note that model M2 has a greater undeformed salt volume in the proximal domain and a smaller salt volume in the distal domain compared to the Espirito Santo margin (Figures 1b and 5). This is a consequence of the relatively high post-salt progradation rate, rapidly burying the more proximal salt and halting its seaward evacuation, which is not observed in nature probably owing to lower post-salt progradation rates (see Section 4.3).

Several wide salt-bearing margins worldwide display a similar margin architecture and styles of salt tectonics as well as magnitudes of extension, translation, shortening, and diapirism as our wide margin model M3. Examples include Campos (Figure 1c) (Davison et al., 2012; do Amarante et al., 2021) and northern Santos in Brazil (Pichel & Jackson, 2020; Pichel et al., 2020), and Lower Congo and Gabon in West Africa (Epin et al., 2021; Kukla et al., 2018; Rowan, 2014; Unternehr et al., 2010). These margins are ∼200–250 km wide and show significant (∼20 km) updip overburden extension that is balanced seaward by translation and downdip shortening (Figure 1c) (cf., Hudec & Jackson, 2004; Quirk et al., 2012; Pichel & Jackson, 2020). The extensional domain along these margins is characterized by large, multi-km offset normal faults and extensional- and expulsion-rollovers (cf., Pichel & Jackson, 2020; Rowan et al., 2022). The intermediate translational domain comprises complex diapirs and asymmetric minibasins, most of which have a multiphase history of reactivation associated with salt flow over base-salt relief (do Amarante et al., 2021; Dooley et al., 2017; 2018; Evans & Jackson, 2020; Peel, 2014). Their downdip domain is characterized by salt inflation, diapir shortening and buckle-folding (Figure 1c). The magnitude of inflation, size, and geometry of these distal diapirs are, however, highly variable between different margin examples. Their distal ends are characterized by allochthonous salt nappes that vary in structural complexity but are broadly of similar width (∼30–40 km) (cf., Davison et al., 2012; Epin et al., 2021; Hudec & Jackson, 2004).

The crustal architecture, style and evolution of salt deformation of our ultra-wide model M4 is similar to the ultra-wide salt-bearing margin segments of West Africa, such as Kwanza, Angola (Figure 1b), and of Brazil, in particular the Santos central segment (Davison et al., 2012; Kukla et al., 2018; Lentini et al., 2010; Pichel

et al., 2020). Other comparable examples include portions of the wider north-central Gulf of Mexico (Hudec et al., 2013, M. P. Jackson & Hudec, 2017; Rowan, 2020). These natural cases present a proximal domain characterized by complex diapirism over partially isolated sub-basins transitioning seaward into an area of pronounced (~30 km) updip extension and development of extensional and/or hybrid rollovers, turtle structures, salt rollers and/or asymmetric minibasins and diapirs (Figure 1b) (Davison et al., 2012; Guerra & Underhill, 2012; Pichel & Jackson, 2020; Pichel et al., 2021). The intermediate domain along these ultra-wide margins is characterized by large areas of complex, multiphase diapirism and overburden translation that broadly balances with updip extension. Their downdip domains present squeezed and complex diapirs passing seaward onto an area of salt inflation, folding and ~30–50 km of salt nappe advance.

4.3. Model Limitations and Future Work

Despite our models comparing well with natural examples, they also contain second-order discrepancies. For example, they do not develop large allochthonous salt canopies and present local variations in salt volume and diapir and minibasin geometries with natural prototypes. These are partially explained because our models are generic, that is, not created to reproduce any specific basin, and because they are 2D and continental rifting and salt flow are essentially 3D processes with significant lateral variability in dynamics and geometries (Brune et al., 2014, 2018; Duclaux et al., 2020; M. P. Jackson & Hudec, 2017; Pichel et al., 2022). Rifting can also involve additional processes not modeled here, such as syn-rift magmatism (e.g., intrusives and SDRs), underplating, hydrothermal activity, and mantle exhumation (cf., Ros et al., 2017; Sapin et al., 2021; Lu & Huismans, 2022; Theunissen & Huismans, 2022). These processes can impact the architecture, rheology, and thermal state of rifted margins and consequently influence salt deposition, its mobility and salt flow. Magmatism may also occur during the post-rift in some of these margins (cf., Magee et al., 2021; do Amarante et al., 2021) and affect the rheology and density structure of both salt and its overburden. Post-rift regional margin uplift is another common process and can change the regional slope of the salt basin as well as increase their post-salt sediment supply into their deep-basin (cf., Hudec & Jackson, 2004; Pichel & Jackson, 2020). Time-dependent post-salt sedimentation rate is also not included in our models. However, sedimentation rate is often variable through time in nature, which is likely to influence salt tectonics.

Our models also do not include intra- or post-salt rheological variabilities, such as for example, intra-salt carbonates, gypsum/anhydrite and/or K-Mg salts, or post-salt carbonates. Non-halite intra-salt lithologies will likely partition intra-salt flow and influence salt mobility and post-salt sediment deformation. Carbonates and anhydrite will reduce salt mobility whereas K-Mg salts are likely to increase it (cf., Dooley et al., 2015; C. A. L. Jackson, Jackson, Hudec, & Rodriguez, 2015; Rowan, 2020). Post-salt carbonates and/or igneous rocks may increase overburden sedimentary load and amplify post-salt minibasin subsidence and diapiric salt flow. All these aspects are also relevant and should therefore be investigated in future research.

5. Conclusions

Our models investigate the interplay between crustal-scale rifted margin architecture, late syn-rift salt deposition, and post-rift salt tectonics for different rifted margin types. We use self-consistent geodynamic modeling to explore factors controlling rifted margin salt tectonics at the scale of the entire margin. The results provide improved understanding of the dynamics and relative timing of rifting and salt deformation, of the factors controlling salt tectonics and post-salt basin architecture, and how these vary for different margin types.

The degree and style of salt tectonics in the models presented is controlled by the interplay of four main factors: (a) the relative rate of post-rift sediment progradation vs. margin width, (b) salt volume, (c) base-salt relief, and (d) salt viscosity.

The relative rate of post-rift sediment progradation versus margin width controls lateral versus vertical salt flow. Low progradation rate to margin width ratio promotes greater overburden translation and lateral salt flow. This results in prominent inclined diapirs, asymmetric minibasins, and significant updip extension and downdip shortening. In contrast, a high progradation rate to margin width ratio inhibits lateral flow and overburden translation resulting in predominantly upright diapirs, symmetrical minibasins, and minor to absent updip extension and downdip contraction.

Salt volume controls the magnitude and variability of salt tectonics, with wider margins accumulating more salt, which leads to more evolved and greater diversity of salt structures.

Base salt relief controls the continuity of the salt basin and the ability of the salt to behave as a single large weak layer below the post-salt prograding sediments, or to be partitioned into a series of individual salt sub-basins. Low base-salt relief, characteristic of wide and ultra-wide rifted margins, promotes linkage of salt tectonics between the proximal, intermediate and distal margin and multi-km seaward salt expulsion and overburden translation associated with complex, multiphase diapirism. In contrast, high base-salt relief, typical for narrow to intermediate width margins, disconnects the salt sub-basins and leads to salt structures restricted to the individual sub-basins and dominantly vertical salt tectonics.

Salt viscosity and the ability for the salt to flow provide a first-order control on the degree and complexity of salt structures. Low salt viscosity promotes greater lateral and vertical salt flow and produces greater complexity of salt tectonic features, whereas high salt viscosity has the opposite effect.

The models presented here are comparable to and explain the variability of salt tectonics for a wide range of rifted margin salt basins in the central South Atlantic, the Gulf of Mexico, and the Red Sea. They can also work as guides to the often-challenging interpretation of subsurface data in these complex settings and to the understanding of their dynamics and the relationship between rifting, continental breakup, salt deposition and tectonics.

Data Availability Statement

All data supporting the findings of this study are contained within the article and Supporting Information S1. Numerical models are computed with published methods and codes described in the Methods and Supporting Information S1. All background data including all model outputs, graphics, and time-steps are presented as Movies S1–S11. They are available for download at the *Dataverse* repository: https://dataverse.no/privateurl.xhtml?token=96a33617-37d8-4e30-a02e-d07b85590afe.

Acknowledgments
We thank the Equinor-UiB Akademia agreement for funding. We thank Uninett Sigma2 for computing time of project NN4704K. We also thank Chris Jackson, Oriol Ferrer, and Frank Peel for the insightful discussions during the development of the numerical models used in this manuscript. We also thank the reviewer Peter Kukla and an anonymous review, and the editor Isabelle Manighetti for the detailed and constructive reviews.

References

Albertz, M., & Ings, S. J. (2012). Some consequences of mechanical stratification in basin-scale numerical models of passive-margin salt tectonics. *Geological Society, London, Special Publications*, *363*(1), 303–330. https://doi.org/10.1144/sp363.14

Allen, J., & Beaumont, C. (2016). Continental margin syn-rift salt tectonics at intermediate width margins. *Basin Research*, *28*(5), 598–633. https://doi.org/10.1111/bre.12123

Allen, J., Beaumont, C., & Deptuck, M. E. (2020). Feedback between synrift lithospheric extension, sedimentation and salt tectonics on wide, weak continental margins. *Petroleum Geoscience*, *26*(1), 16–35.

Andrés-Martínez, M., Pérez-Gussinyé, M., Armitage, J., & Morgan, J. P. (2019). Thermomechanical implications of sediment transport for the architecture and evolution of continental rifts and margins. *Tectonics*, *38*(2), 641–665. https://doi.org/10.1029/2018tc005346

Baby, G., Guillocheau, F., Braun, J., Robin, C., & Dall'Asta, M. (2020). Solid sedimentation rates history of the Southern African continental margins: Implications for the uplift history of the South African Plateau. *Terra Nova*, *32*(1), 53–65. https://doi.org/10.1111/ter.12435

Blaich, O. A., Faleide, J. I., & Tsikalas, F. (2011). Crustal breakup and continent-ocean transition at South Atlantic conjugate margins. *Journal of Geophysical Research*, *116*(B1), B01402. https://doi.org/10.1029/2010jb007686

Brune, S., Heine, C., Pérez-Gussinyé, M., & Sobolev, S. V. (2014). Rift migration explains continental margin asymmetry and crustal hyper-extension. *Nature Communications*, *5*(1), 1–9. https://doi.org/10.1038/ncomms5014

Brune, S., Williams, S. E., Butterworth, N. P., & Müller, R. D. (2016). Abrupt plate accelerations shape rifted continental margins. *Nature*, *536*(7615), 201–204.

Brune, S., Williams, S. E., & Müller, R. D. (2018). Oblique rifting: The rule, not the exception. *Solid Earth*, *9*(5), 1187–1206. https://doi.org/10.5194/se-9-1187-2018

Buck, W. R. (1991). Modes of continental lithospheric extension. *Journal of Geophysical Research*, *96*(B12), 20161–20178. https://doi.org/10.1029/91jb01485

Carter, N. L., Horseman, S. T., Russell, J. E., & Handin, J. (1993). Rheology of rocksalt. *Journal of Structural Geology*, *15*(9–10), 1257–1271. https://doi.org/10.1016/0191-8141(93)90168-a

Curry, M. A., Peel, F. J., Hudec, M. R., & Norton, I. O. (2018). Extensional models for the development of passive-margin salt basins, with application to the Gulf of Mexico. *Basin Research*, *30*(6), 1180–1199. https://doi.org/10.1111/bre.12299

Davison, I., Anderson, L., & Nuttall, P. (2012). Salt deposition, loading and gravity drainage in the Campos and Santos salt basins. *Geological Society of London Special Publications*, *363*(1), 159–174. https://doi.org/10.1144/sp363.8

Deptuck, M. E., & Kendell, K. L. (2017). A review of Mesozoic-Cenozoic salt tectonics along the Scotian margin, eastern Canada. *Permo-Triassic Salt Provinces of Europe, North Africa and the Atlantic Margins* (pp. 287–312).

do Amarante, F. B., Jackson, C. A. L., Pichel, L. M., Scherer, C. M. D. S., & Kuchle, J. (2021). Pre-salt rift morphology controls salt tectonics in the Campos Basin, offshore SE Brazil. *Basin Research*, *33*(5), 2837–2861. https://doi.org/10.1111/bre.12588

Dooley, T. P., Hudec, M. R., Carruthers, D., Jackson, M. P., & Luo, G. (2017). The effects of base-salt relief on salt flow and suprasalt deformation patterns—Part 1: Flow across simple steps in the base of salt. *Interpretation*, *5*(1), SD1–SD23. https://doi.org/10.1190/int-2016-0087.1

Dooley, T. P., Hudec, M. R., Pichel, L. M., & Jackson, M. P. (2018). The impact of base-salt relief on salt flow and suprasalt deformation patterns at the autochthonous, paraautochthonous and allochthonous level: Insights from physical models. *Geological Society, London, Special Publications*, *476*(1), 287–315. https://doi.org/10.1144/sp476.13

Dooley, T. P., Jackson, M. P., Jackson, C. A. L., Hudec, M. R., & Rodriguez, C. R. (2015). Enigmatic structures within salt walls of the Santos Basin—Part 2: Mechanical explanation from physical modelling. *Journal of Structural Geology*, *75*, 163–187. https://doi.org/10.1016/j.jsg.2015.01.009

Duclaux, G., Huismans, R. S., & May, D. A. (2020). Rotation, narrowing, and preferential reactivation of brittle structures during oblique rifting. *Earth and Planetary Science Letters*, *531*, 115952. https://doi.org/10.1016/j.epsl.2019.115952

Epin, M. E., Manatschal, G., Sapin, F., & Rowan, M. G. (2021). The tectono-magmatic and subsidence evolution during lithospheric breakup in a salt-rich rifted margin: Insights from a 3D seismic survey from southern Gabon. *Marine and Petroleum Geology*, *128*, 105005. https://doi.org/10.1016/j.marpetgeo.2021.105005

Erdős, Z., Huismans, R. S., van der Beek, P., & Thieulot, C. (2014). Extensional inheritance and surface processes as controlling factors of mountain belt structure. *Journal of Geophysical Research: Solid Earth*, *119*(12), 9042–9061. https://doi.org/10.1002/2014jb011408

Evans, S. L., & Jackson, C. A. L. (2020). Base-salt relief controls salt-related deformation in the Outer Kwanza Basin, offshore Angola. *Basin Research*, *32*(4), 668–687. https://doi.org/10.1111/bre.12390

Gemmer, L., Ings, S. J., Medvedev, S., & Beaumont, C. (2004). Salt tectonics driven by differential sediment loading: Stability analysis and finite-element experiments. *Basin Research*, *16*(2), 199–218. https://doi.org/10.1111/j.1365-2117.2004.00229.x

Gleason, G. C., & Tullis, J. (1995). A flow law for dislocation creep of quartz aggregates determined with the molten salt cell. *Tectonophysics*, *247*(1–4), 1–23. https://doi.org/10.1016/0040-1951(95)00011-b

Goteti, R., Beaumont, C., & Ings, S. J. (2013). Factors controlling early stage salt tectonics at rifted continental margins and their thermal consequences. *Journal of Geophysical Research: Solid Earth*, *118*(6), 3190–3220. https://doi.org/10.1002/jgrb.50201

Gradmann, S., & Beaumont, C. (2017). Numerical modelling study of mechanisms of mid-basin salt canopy evolution and their potential applications to the Northwestern Gulf of Mexico. *Basin Research*, *29*(4), 490–520. https://doi.org/10.1111/bre.12186

Guerra, M. C., & Underhill, J. R. (2012). Role of halokinesis in controlling structural styles and sediment dispersal in the Santos Basin, offshore Brazil. *Geological Society, London, Special Publications*, *363*(1), 175–206. https://doi.org/10.1144/sp363.9

Hudec, M. R., & Jackson, M. P. (2004). Regional restoration across the Kwanza Basin, Angola: Salt tectonics triggered by repeated uplift of a metastable passive margin. *AAPG Bulletin*, *88*(7), 971–990. https://doi.org/10.1306/02050403061

Hudec, M. R., & Norton, I. O. (2019). Upper Jurassic structure and evolution of the Yucatán and Campeche subbasins, southern Gulf of Mexico. *AAPG Bulletin*, *103*(5), 1133–1151. https://doi.org/10.1306/11151817405

Hudec, M. R., Norton, I. O., Jackson, M. P., & Peel, F. J. (2013). Jurassic evolution of the Gulf of Mexico salt basin. *AAPG Bulletin*, *97*(10), 1683–1710. https://doi.org/10.1306/04011312073

Huismans, R. S., & Beaumont, C. (2002). Asymmetric lithospheric extension: The role of frictional plastic strain softening inferred from numerical experiments. *Geology*, *30*(3), 211–214. https://doi.org/10.1130/0091-7613(2002)030<0211:aletro>2.0.co;2

Huismans, R. S., & Beaumont, C. (2003). Symmetric and asymmetric lithospheric extension: Relative effects of frictional-plastic and viscous strain softening. *Journal of Geophysical Research*, *108*(B10). https://doi.org/10.1029/2002jb002026

Huismans, R. S., & Beaumont, C. (2011). Depth-dependent extension, two-stage breakup and cratonic underplating at rifted margins. *Nature*, *473*(7345), 74–78. https://doi.org/10.1038/nature09988

Huismans, R. S., & Beaumont, C. (2014). Rifted continental margins: The case for depth-dependent extension. *Earth and Planetary Science Letters*, *407*, 148–162. https://doi.org/10.1016/j.epsl.2014.09.032

Izquierdo-Llavall, E., Ringenbach, J. C., Sapin, F., Rives, T., & Callot, J. P. (2022). Crustal structure and lateral variations in the Gulf of Mexico conjugate margins: From rifting to break-up. *Marine and Petroleum Geology*, *136*, 105484. https://doi.org/10.1016/j.marpetgeo.2021.105484

Jackson, C. A. L., Jackson, M. P., & Hudec, M. R. (2015). Understanding the kinematics of salt-bearing passive margins: A critical test of competing hypotheses for the origin of the Albian Gap, Santos Basin, offshore Brazil. *Bulletin*, *127*(11–12), 1730–1751. https://doi.org/10.1130/b31290.1

Jackson, C. A. L., Jackson, M. P., Hudec, M. R., & Rodriguez, C. R. (2015). Enigmatic structures within salt walls of the Santos Basin—Part 1: Geometry and kinematics from 3D seismic reflection and well data. *Journal of Structural Geology*, *75*, 135–162. https://doi.org/10.1016/j.jsg.2015.01.010

Jackson, M. P., & Hudec, M. R. (2017). *Salt tectonics: Principles and practice*. Cambridge University Press.

Karato, S.-I., & Wu, P. (1993). Rheology of the upper mantle: A synthesis. *Science*, *260*(5109), 771–778. https://doi.org/10.1126/science.260.5109.771

Kukla, P. A., Strozyk, F., & Mohriak, W. U. (2018). South Atlantic salt basins–witnesses of complex passive margin evolution. *Gondwana Research*, *53*, 41–57. https://doi.org/10.1016/j.gr.2017.03.012

Lavier, L. L., & Manatschal, G. (2006). A mechanism to thin the continental lithosphere at magma-poor margins. *Nature*, *440*(7082), 324–328. https://doi.org/10.1038/nature04608

Lentini, M. R., Fraser, S. I., Sumner, H. S., & Davies, R. J. (2010). Geodynamics of the central South Atlantic conjugate margins: Implications for hydrocarbon potential. *Petroleum Geoscience*, *16*(3), 217–229. https://doi.org/10.1144/1354-079309-909

Lu, G., & Huismans, R. S. (2022). Magmatism at passive margins: Effects of depth-dependent wide rifting and lithospheric counterflow. *Journal of Geophysical Research: Solid Earth*, *127*(3), e2021JB023046. https://doi.org/10.1029/2021jb023046

Magee, C., Pichel, L. M., Madden-Nadeau, A. L., Jackson, C. A. L., & Mohriak, W. (2021). Salt–magma interactions influence intrusion distribution and salt tectonics in the Santos Basin, offshore Brazil. *Basin Research*, *33*(3), 1820–1843. https://doi.org/10.1111/bre.12537

Marton, L. G., Tari, G. C., & Lehmann, C. T. (2000). Evolution of the Angolan passive margin, West Africa, with emphasis on post-salt structural styles. *Geophysical Monograph-American Geophysical Union*, *115*, 129–150.

McKenzie, D. (1978). Some remarks on the development of sedimentary basins. *Earth and Planetary Science Letters*, *40*(1), 25–32. https://doi.org/10.1016/0012-821x(78)90071-7

Mohriak, W. U., & Leroy, S. (2013). Architecture of rifted continental margins and break-up evolution: Insights from the South Atlantic, North Atlantic and Red Sea–Gulf of Aden conjugate margins. *Geological Society, London, Special Publications*, *369*(1), 497–535. https://doi.org/10.1144/sp369.17

Peel, F. J. (2014). The engines of gravity-driven movement on passive margins: Quantifying the relative contribution of spreading vs. gravity sliding mechanisms. *Tectonophysics*, *633*, 126–142. https://doi.org/10.1016/j.tecto.2014.06.023

Peel, F. J., Travis, C. J., & Hossack, J. R. (1995). Genetic structural provinces and salt tectonics of the Cenozoic offshore US Gulf of Mexico: A preliminary analysis. In M. P. A. Martin, D. G. Roberts, & S. Snelson (Eds.), *Salt tectonics: A global perspective* (Vol. 65, pp. 153–175). AAPG Memoir.

Pichel, L. M., Huismans, R. S., Gawthorpe, R. L., Faleide, J. I., & Theunissen, T. (2022). Late-Syn- to post-rift salt tectonics on wide rifted margins—Insights from geodynamic modelling. *Tectonics*, *41*(8), e2021TC007158. https://doi.org/10.1029/2021TC007158

Pichel, L. M., Huuse, M., Redfern, J., & Finch, E. (2019). The influence of base-salt relief, rift topography and regional events on salt tectonics offshore Morocco. *Marine and Petroleum Geology*, *103*, 87–113. https://doi.org/10.1016/j.marpetgeo.2019.02.007

Pichel, L. M., & Jackson, C. A. L. (2020). The enigma of the Albian Gap: Spatial variability and the competition between salt expulsion and extension. *Journal of the Geological Society*, *177*(6), 1129–1148. https://doi.org/10.1144/jgs2020-055

Pichel, L. M., Jackson, C. A. L., Peel, F., & Dooley, T. P. (2020). Base-salt relief controls salt-tectonic structural style, São Paulo Plateau, Santos Basin, Brazil. *Basin Research*, *32*(3), 453–484. https://doi.org/10.1111/bre.12375

Pichel, L. M., Jackson, C. A. L., Peel, F., & Ferrer, O. (2021). The Merluza Graben: How a failed spreading center influenced margin structure, and salt deposition and tectonics in the Santos Basin, Brazil. *Tectonics*, *40*(10), e2020TC006640. https://doi.org/10.1029/2020tc006640

Pichel, L. M., Peel, F., Jackson, C. A.-L., & Huuse, M. (2018). Geometry and kinematics of salt-detached ramp syncline basins. *Journal of Structural Geology*, *115*, 208–230. https://doi.org/10.1016/j.jsg.2018.07.016

Quirk, D. G., Schødt, N., Lassen, B., Ings, S. J., Hsu, D., Hirsch, K. K., & Von Nicolai, C. (2012). Salt tectonics on passive margins: Examples from Santos, Campos and Kwanza basins. *Geological Society, London, Special Publications*, *363*(1), 207–244. https://doi.org/10.1144/sp363.10

Rodriguez, C. R., Jackson, C. L., Rotevatn, A., Bell, R. E., & Francis, M. (2018). Dual tectonic-climatic controls on salt giant deposition in the Santos Basin, offshore Brazil. *Geosphere*, *14*(1), 215–242. https://doi.org/10.1130/ges01434.1

Ros, E., Pérez-Gussinyé, M., Araújo, M., Thoaldo Romeiro, M., Andrés-Martínez, M., & Morgan, J. P. (2017). Lower crustal strength controls on melting and serpentinization at magma-poor margins: Potential implications for the South Atlantic. *Geochemistry, Geophysics, Geosystems*, *18*(12), 4538–4557. https://doi.org/10.1002/2017GC007212

Rowan, M. G. (2014). Passive-margin salt basins: Hyperextension, evaporite deposition, and salt tectonics. *Basin Research*, *26*(1), 154–182. https://doi.org/10.1111/bre.12043

Rowan, M. G. (2020). The South Atlantic and Gulf of Mexico salt basins: Crustal thinning, subsidence and accommodation for salt and presalt strata. *Geological Society, London, Special Publications*, *476*(1), 333–363. https://doi.org/10.1144/sp476.6

Rowan, M. G., Tilton, J., Lebit, H., & Fiduk, J. C. (2022). Thin-skinned extensional salt tectonics, counterregional faults, and the Albian Gap of Brazil. *Marine and Petroleum Geology*, *137*, 105478. https://doi.org/10.1016/j.marpetgeo.2021.105478

Rowan, M. G., Urai, J. L., Fiduk, J. C., & Kukla, P. A. (2019). Deformation of intrasalt competent layers in different modes of salt tectonics. *Solid Earth*, *10*(3), 987–1013. https://doi.org/10.5194/se-10-987-2019

Sapin, F., Ringenbach, J. C., & Clerc, C. (2021). Rifted margins classification and forcing parameters. *Scientific Reports*, *11*(1), 1–17. https://doi.org/10.1038/s41598-021-87648-3

Spiers, C. J., Schutjens, P. M. T. M., Brzesowsky, R. H., Peach, C. J., Liezenberg, J. L., & Zwart, H. J. (1990). Experimental determination of constitutive parameters governing creep of rocksalt by pressure solution. *Geological Society, London, Special Publications*, *54*(1), 215–227. https://doi.org/10.1144/gsl.sp.1990.054.01.21

Tari, G., Brown, D., Jabou, H., Hafid, M., Loudenk, K., & Zizi, M. (2012). The conjugate margins of Morocco and Nova Scotia. *Regional geology and tectonics: Phanerozoic passive margins, cratonic basins and global tectonic maps* (p. 285).

Tari, G., Molnar, J., & Ashton, P. (2003). Examples of salt tectonics from West Africa: A comparative approach. *Geological Society, London, Special Publications*, *207*(1), 85–104. https://doi.org/10.1144/gsl.sp.2003.207.5

Tari, G., Novotny, B., Jabour, H., & Hafid, M. (2017). Salt tectonics along the Atlantic margin of NW Africa (Morocco and Mauritania). In *Permo-Triassic Salt Provinces of Europe, North Africa and the Atlantic Margins* (pp. 331–351). Elsevier.

Theunissen, T., & Huismans, R. S. (2019). Long-term coupling and feedback between tectonics and surface processes during non-volcanic rifted margin formation. *Journal of Geophysical Research: Solid Earth*, *124*(11), 12323–12347. https://doi.org/10.1029/2018jb017235

Theunissen, T., & Huismans, R. S. (2022). Mantle exhumation at magma-poor rifted margins controlled by frictional shear zones. *Nature Communications*, *13*(1), 1–12. https://doi.org/10.1038/s41467-022-29058-1

Thieulot, C. (2011). FANTOM: Two-and three-dimensional numerical modelling of creeping flows for the solution of geological problems. *Physics of the Earth and Planetary Interiors*, *188*(1–2), 47–68. https://doi.org/10.1016/j.pepi.2011.06.011

Unternehr, P., Péron-Pinvidic, G., Manatschal, G., & Sutra, E. (2010). Hyper-extended crust in the South Atlantic: In search of a model.

Van Keken, P. E., Spiers, C. J., Van den Berg, A. P., & Muyzert, E. J. (1993). The effective viscosity of rocksalt: Implementation of steady-state creep laws in numerical models of salt diapirism. *Tectonophysics*, *225*(4), 457–476. https://doi.org/10.1016/0040-1951(93)90310-g

Wolf, L., Huismans, R. S., Rouby, D., Robert, L., Gawthorpe, R. L., & Wolf, S. G. (2022). Links between faulting, topography, and sediment production during continental rifting: Insights from coupled surface process, thermomechanical modeling. *Journal of Geophysical Research: Solid Earth*, *127*(3), e2021JB023490. https://doi.org/10.1029/2021jb023490

Zalán, P. V., Severino, M. D. C., Rigoti, C. A., Magnavita, L. P., Oliveira, J. A. B., & Vianna, A. R. (2011). An entirely new 3D-view of the crustal and mantle structure of a South Atlantic passive margin–Santos, Campos and Espírito Santo basins, Brazil. In *AAPG annual conference and exhibition* (Vol. *10*, p. 13).

References From the Supporting Information

Buck, W. R. (1993). Effect of lithospheric thickness on the formation of high-and low-angle normal faults. *Geology*, *21*(10), 933–936. https://doi.org/10.1130/0091-7613(1993)021<0933:eoltot>2.3.co;2

Lavier, L. L., Buck, W. R., & Poliakov, A. N. (2000). Factors controlling normal fault offset in an ideal brittle layer. *Journal of Geophysical Research*, *105*(B10), 23431–23442. https://doi.org/10.1029/2000jb900108

Lavier, L. L., Roger Buck, W., & Poliakov, A. N. (1999). Self-consistent rolling-hinge model for the evolution of large-offset low-angle normal faults. *Geology*, *27*(12), 1127–1130. https://doi.org/10.1130/0091-7613(1999)027<1127:scrhmf>2.3.co;2

Pysklywec, R. N., & Beaumont, C. (2004). Intraplate tectonics: Feedback between radioactive thermal weakening and crustal deformation driven by mantle lithosphere instabilities. *Earth and Planetary Science Letters*, *221*(1–4), 275–292. https://doi.org/10.1016/s0012-821x(04)00098-6

Willett, S. D. (1992). Dynamic and kinematic growth and change of a Coulomb wedge. In K. R. McClay (Ed.), *Thrust tectonics* (pp. 19–31). Springer Netherlands. https://doi.org/10.1007/978-94-011-3066-0